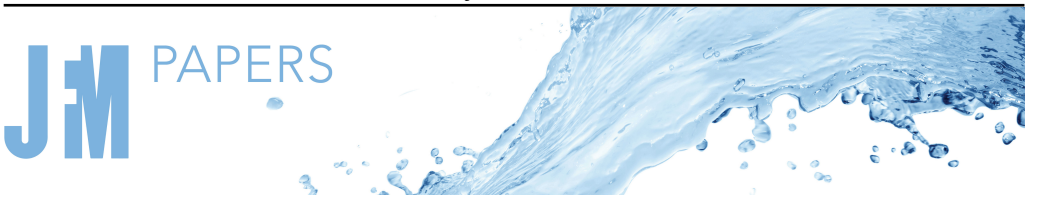
J. Fluid Mech. (2026), *vol.* 1041, A26, doi:10.1017/jfm.2026.11936



Flow-structure effects on auto-ignition processes of supersonic hydrogen–air mixing layers

Nereida G. De Codina[1,2], **Pedro J. Martínez-Ferrer**[3,2], **Daniel Mira**[2], **Cesar Huete**[4] **and Daniel Martínez-Ruiz**[1]

[1]ETSI Aeronáutica y del Espacio, Universidad Politécnica de Madrid, Madrid 28040, Spain

[2]Barcelona Supercomputing Center, Barcelona, Spain

[3]Universitat Politècnica de Catalunya – BarcelonaTech (UPC), Barcelona, Spain

[4]Departamento de Ingeniería Térmica y de Fluidos, Universidad Carlos III de Madrid, Leganés 28911, Spain

Corresponding author: Daniel Martínez-Ruiz, daniel.mruiz@upm.es

(Received 22 January 2026 UTC; revised 21 May 2026 UTC; accepted 16 July 2026 UTC)

This work presents a numerical study of supersonic hydrogen–air mixing layers, in both shock-free and shock-assisted configurations, using high-fidelity simulations performed with the computational fluid dynamics solver CREAMS, which includes detailed diffusion transport and chemical kinetics. The canonical two-dimensional mixing layer is analysed to assess the influence of inlet profiles and shock-induced flow structures on auto-ignition behaviour. In the absence of shocks, self-similar inlet profiles – accounting for Soret, Dufour and viscous dissipation effects – exhibit distinct ignition characteristics compared to standard hyperbolic tangent profiles. For non-isothermal (hot–cold) streams, the ignition distance remains nearly unaffected by the inlet profile, confirming a primarily thermal control of ignition; however, the ignition kernel shifts towards the hotter stream due to enhanced species diffusion. In contrast, for isothermal configurations, the self-similar profile significantly accelerates ignition, reducing the ignition distance by over 1 cm, primarily through viscous heating effects. Under shock impingement conditions, increasing the incident shock angle strengthens the reflected expansion wave, locally cooling the upper stream and delaying ignition, with complete ignition failure observed for sufficiently low inclined shocks. Near marginal conditions, only the self-similar profile sustains stable ignition by promoting higher initial mixedness. The results provide a detailed database and physical insight into how inlet thermochemical structure and

© The Author(s), 2026. Published by Cambridge University Press. This is an Open Access article, distributed under the terms of the Creative Commons Attribution licence (https://creativecommons.org/licenses/by/4.0/), which permits unrestricted re-use, distribution and reproduction, provided the original article is properly cited.

https://doi.org/10.1017/jfm.2026.11936 Published online by Cambridge University Press

shock–mixing layer interactions govern ignition distances and flame stabilisation in supersonic reactive flows.

Key words: shock waves, combustion

1. Introduction

Hypersonic air-breathing vehicles offer the potential for rapid global civil transport, quick-strike defence capabilities, and efficient space transportation of payloads to low Earth orbit (Urzay 2018). However, technical challenges arise in capturing and combusting atmospheric air at hypersonic speeds. As flight speed increases, drag forces rise, and the airflow shorter residence time in the combustor hinders the mixing and combustion processes needed for efficient propulsion.

In the late 1950s, the central debate of the community concerning the chemical heat release mechanisms in a supersonic stream confronted two modes of combustion: detonations, controlled by a wave mechanism (Gross & Chinitz 1960), and supersonic diffusion flames, controlled by the turbulent mixing process of the reactants (Libby 1962; Da Riva *et al.* 1964; Ferri *et al.* 1964). The first main difference between the proposed modes of combustion was the catastrophically high total pressure loss in planar detonations compared to the shock-free combustion of diffusion-controlled flames. Second, the concentrated pressure rise in detonations promoted the flow choking, while gradually distributed heat in the diffusion flame enabled the flow to remain supersonic.

In modern scramjets, air is compressed using an intake-isolator system, avoiding the need for rotating components, and directed into the combustor where fuel burns in supersonic diffusion flames. This results in an extremely short residence time – often just fractions of a millisecond – which makes it difficult for fuel and air to mix thoroughly and achieve effective combustion. As a result, ignition cannot typically rely solely on diffusion and heat conduction (Gutmark *et al.* 1995), necessitating more complex configurations. It has been suggested that appropriately positioned shock waves within the combustion chamber can assist by heating the mixture and accelerating the mixing process (Marble 1994). This effect arises partly from the inherent temperature increase across the shock wave, and partly from the interaction of the shock with the non-uniform flow (Brummund & Nuding 1997; Tang *et al.* 2024*a*). The isolator serves as a buffer to prevent shock waves generated within the combustor from disrupting the intake flow, ensuring stable airflow (Liu *et al.* 2020). Shock waves there affect the flow near the walls, causing a sudden transition to turbulence and increased wall heating within boundary layers (Gaitonde 2015; Gaitonde & Adler 2023). These factors ultimately influence the flow conditions at the entrance of the combustor, and therefore, the combustion process. The highest computational demands still arise within the combustor itself, since accurately describing the complete combustion domain requires modelling turbulence, detailed transport properties, and chemical kinetics, with fuel and oxidiser mixing at the molecular level (Abdulrahman *et al.* 2023), which result in a wide disparity of spatio-temporal scales (Tang *et al.* 2024*b*). As a result, numerical simulations of scramjet combustion systems are conducted independently of previous stages, and rely heavily on accurate inlet conditions. It is clear that the level of uncertainty in the properties of airflow, previously compressed by multiple shock waves, entering the combustion chamber is very high, and their impact on the combustion process requires comprehensive studies on the inlet conditions in the computational domain.

https://doi.org/10.1017/jfm.2026.11936 Published online by Cambridge University Press

In the case of planar co-flow injection systems, ignition depends on the mixing and heating of parallel supersonic streams of fuel and oxidiser. Various numerical studies have provided critical insights into the dynamics and flow structure of supersonic mixing layers (Sandham & Reynolds 1989; Leep *et al.* 1993; Kourta & Sauvage 2002), where the convective Mach number M_c, representing the speed of relative motion between the two streams normalised by the average speed of sound, plays a critical role in governing the dynamics, along with the characteristic Reynolds number Re. Specifically, higher values of M_c typically result in reduced turbulent intensity within the mixing layer, as compressibility dampens the turbulence (Barre *et al.* 1994; Sarkar 1995; Barre & Bonnet 2015). Recently, high-fidelity simulations have highlighted the persistent influence of molecular diffusion, compressibility and turbulence–chemistry coupling. Collectively, these works (Qiao *et al.* 2025; Tian *et al.* 2025; Wei *et al.* 2025; Xie *et al.* 2025) demonstrate that differential diffusion effects remain relevant even in turbulence-dominated regimes, that compressibility modulates scalar transport and mixing efficiency, and that improved modelling approaches, such as Lagrangian filtered mass density function formulations, enhance the prediction of reacting flow dynamics.

When the two streams consist of reactive gases, an additional time scale or convective length related to the chemical process emerges, which allows the definition of a characteristic Damköhler number Da (Drummond 1988; Menon & Fernando 1990; Ju & Niioka 1994; Nishioka & Law 1997). In the context of auto-igniting H_2–air parallel streams, the inlet profile choice additionally includes temperature distributions alongside species concentrations. This aspect is particularly critical due to the high temperature sensitivity of radical-promoting elementary reactions in H_2–air reactive systems, which largely dictate the location of the ignition kernel within the reactive mixing layer. Moreover, although auto-ignition processes are fundamentally influenced by the prevailing temperature, pressure may have a pivotal impact in the chemical kinetics. In fact, at pressures ranging from 1 to 100 atm, the crossover temperature varies between approximately 950 and 1500 K (Sánchez & Williams 2014).

Moreover, the impingement of shock waves on co-flow configurations has been extensively investigated in previous works (Moeckel 1952; Buttsworth 1996; Martínez-Ruiz *et al.* 2018), as it is known to substantially modify the local flow structure and thermodynamic state. In configurations where oblique shocks interact with reactive mixing layers, the resulting local increases in pressure and temperature can drastically alter the ignition dynamics, making the prediction of ignition onset and location particularly challenging (Huete *et al.* 2015 and Huete *et al.* 2017; Zhang *et al.* 2021; Boukharfane 2025; Yu & Chen 2025). Building upon these findings, the present work aims to isolate and quantify the individual effects of shock-induced flow structures on the auto-ignition behaviour of supersonic hydrogen–air mixing layers.

This study examines the impact of different inner profiles of state variables on the ignition distance in a supersonic H_2 mixing layer, under both shock-free and shock-assisted conditions. The effect of different computational inflow distributions was previously analysed in non-reactive subsonic mixing layers (McMullan *et al.* 2007). Here, inlet conditions consist of (i) hyperbolic functions that match the external velocity, temperature and species profiles, and (ii) inlet conditions derived from self-similar functions that emulate the coherent evolution of the mixing layer, originating from a virtual point at a zero-thickness splitter plate. The latter provide a more realistic thermochemical structure than the commonly used hyperbolic tangent profiles. The shock-free cases are analysed for both same-temperature external H_2–air streams and configurations with a hotter air stream. For the latter condition, since the ignition kernel is located in the hot edge of the mixing layer, the auto-ignition distance occurs at the same distance regardless of the form

https://doi.org/10.1017/jfm.2026.11936 Published online by Cambridge University Press

of the inlet conditions. When isothermal conditions are considered, self-similar profiles predict much shorter distances, because ignition is triggered by the inner shear-induced temperature peak placed far from the upper edge that has an impact on the species mass fractions due to the Soret effect. Comparison of these profiles reveals that auto-ignition not only is governed by bulk parameters, but is highly sensitive to the internal thermochemical variations of the mixing layer at the inlet. For the oblique shock evaluation, various impingement angles are analysed while maintaining post-shock temperatures constant and equal to those in shock-free conditions. This approach isolates shock-induced flow structures to assess their impact on the ignition event. The results presented throughout this paper highlight the competing roles of mixing, viscous heating and compressibility, demonstrating that inlet flow structure can decisively influence ignition dynamics.

The remainder of the paper is structured as follows. Section 2 presents the external flow configuration and the theoretical insight on the inner region of the mixing layer. Then § 3 details the numerical set-up employed for the study. Section 4 is devoted to the reference shock-free configurations, where the auto-ignition distance is evaluated in four different inlet conditions. Section 5 addresses the shock-assisted ignition configuration, prior to the conclusions in § 6.

2. Supersonic reacting mixing layers

The main objective of this study is to provide further understanding of the behaviour of the auto-ignition of a supersonic reactive flow, subject to the modification of inlet conditions and incidence of oblique shock waves, through two-dimensional direct numerical simulations (DNS). Although we recognise that the three-dimensional evolution of turbulent mixing layers may be of the utmost importance for mixing characterisation, we will first focus on the thermochemical effects and first-order flow dynamics produced by shock waves and thermal expansion processes, relegating specific turbulence dynamics to future studies, and reducing the analysis to two-dimensional flows; this implies that inherently three-dimensional mechanisms, such as vortex stretching, the full turbulence cascade, and associated small-scale intermittency, are not considered in this study.

Figure 1(*a*) shows the characteristic domain of study for a supersonic co-flow, regardless of the geometry and constraints of the devices enclosing the reactive layer. Therefore, the physical problem must be prescribed by the properties of the upper (subscript 1) and lower (subscript 2) streams. In particular, the characteristic parameters of the mixing layer in absence of the impinging shock are the Mach numbers M_1, M_2, temperatures T_1, T_2, and compositions $Y_{1\alpha}$, $Y_{2\alpha}$ of the streams. The mixture is, in turn, influenced by the initial vorticity thickness of the mixing layer δ^0_ω, as it indirectly defines the distance x_0 of the domain inlet to a virtual origin (e.g. a splitter plate). This scaling thickness defines the development of the diffusive effects of species (mass), thermal transfer (heat) and viscosity (momentum shear). The auto-ignition behaviour herein is controlled by the competition between chemical kinetics along with pressure, mass diffusion and thermal mixing effects in compressible flows, considering detailed transport and chemical kinetics.

First, a reactive co-flow configuration in the absence of oblique shock impingement is considered as reference. Specifically, this base-case problem nearly mimics the experimental conditions of Cheng *et al.* (1994), conformed by an upper stream of $M_1 = 2.0$ corresponding to vitiated air ($Y_{O_2} = 0.2448$, $Y_{H_2O} = 0.1748$, $Y_{N_2} = 0.5799$) and temperature $T_1 = 1250$ K, and a lower stream of pure hydrogen at Mach number $M_2 = 1.25$ and temperature $T_2 = 545$ K, on a planar mixing layer configuration. These conditions are consistent with those encountered in practical high-speed propulsion systems. For example, experimental configurations such as HyShot-II report inlet air temperatures in

https://doi.org/10.1017/jfm.2026.11936 Published online by Cambridge University Press

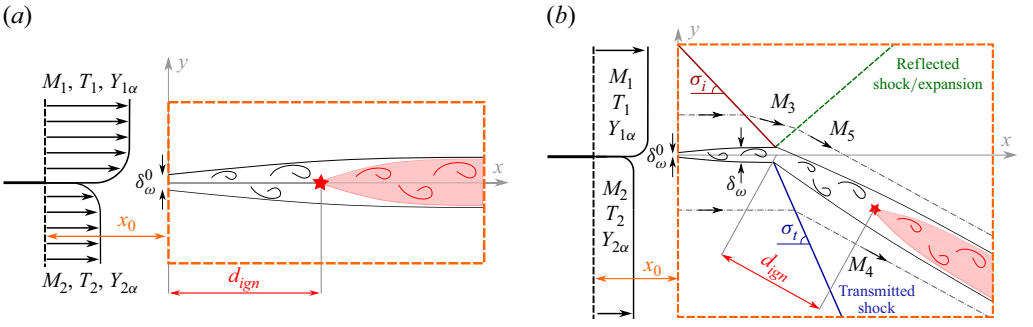


Figure 1. Sketch and parameters of the two-dimensional computational domain for (*a*) a supersonic mixing layer, and (*b*) an oblique shock-impinging mixing layer.

the range 1000−1400 K and Mach numbers between 2.4 and 3.2. Although hydrogen injection typically occurs near sonic conditions at lower initial temperatures (300 K) (Nordin-Bates *et al.* 2017; Urzay 2018), the elevated temperatures considered in this study are also representative of regenerative cooling strategies in scramjet engines, where the fuel can reach temperatures of the order of 900–1000 K prior to injection (Tsujikawa & Northam 1996; Bao *et al.* 2014).

Second, the description of shock impingement effects incorporates the interaction of various wave structures, and their prescribed intensity, with the auto-ignition process of the supersonic mixing layer. Specifically, the characteristic supersonic expansions that arise as reflected structures can locally cool down the reactive mixture, delaying the initiation of the chemical reaction.

2.1. *Ideal shock–refraction equilibrium*

When an oblique shock wave impinges on a tangential discontinuity – such as a shear or mixing layer – it gets refracted, resulting in a transmitted shock and a reflected wave, as depicted in the sketch of figure 1(*b*). In general, the two post-shock streams (subscripts 3 and 4 for top and bottom, respectively) have different pressures and streamline deflections. Then an additional reflected wave (either an expansion or a shock) is responsible for providing additional deflection and pressure changes (subscript 5) to grant the mechanical equilibrium in the tangential discontinuity between regions 4 and 5 downstream (Landau & Lifshitz 1966). Depending on the initial values of the Mach numbers M_1, M_2, as well as the angle of inclination of the incident shock σ_i, different regimes are found.

Figure 2 depicts the Mach number and shock angle domain, bounded by a lower limit of supersonic flow normal component ($M_1 \sin\sigma_i = 1$) as a solid black line. For a given value of the upper-stream Mach number M_1 and oblique shock incident angle σ_i, shown with a blue circle in figure 2(*a*), a family of possible combinations of M_2 enables the global mechanical equilibrium with different values of the transmitted shock angle σ_t. Three different regular configurations can be attained: (i) a reflected expansion (points lying on the blue solid curve); (ii) a reflected shock (on the red dashed curve); or (iii) a neutral transmission with no additional reflected wave, either for $M_2 = M_1$ and $\sigma_t = \sigma_i$ or at the other transition point from reflected expansion to shock. Nevertheless, this group of regular solutions defines a critical Mach number M_{cr} (dash-dotted vertical line), below which a stable configuration cannot be reached. Irregular configurations may arise from the interaction between a shock wave and a mixing layer if, given a set M_1 and σ_i, a value of $M_2 < M_{cr}$ is used at the other stream. In fact, an irregular structure is formed when

https://doi.org/10.1017/jfm.2026.11936 Published online by Cambridge University Press

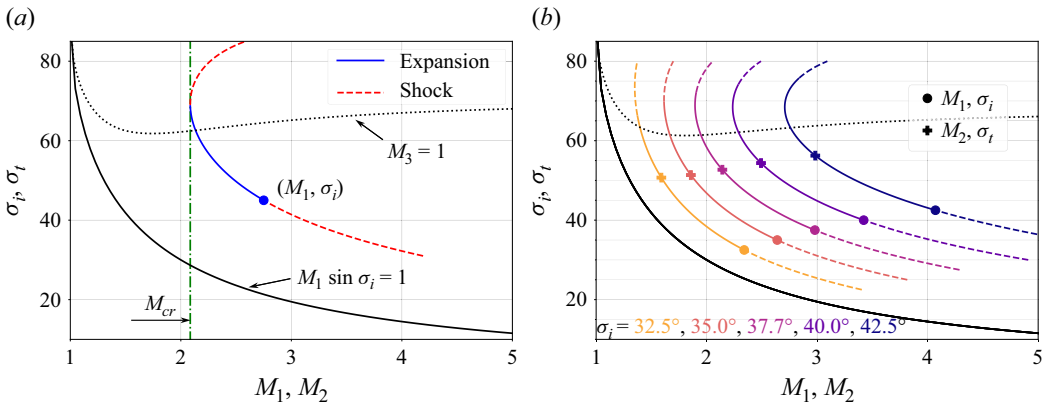


Figure 2. (*a*) Continuous set of ideal flow solutions with mechanical equilibrium (blue and red curves) of an oblique shock over a tangential discontinuity. (*b*) Combinations of upstream parameters M_1, M_2, σ_i that provide post-shock Mach numbers equal to the base-case flow.

the reflected shock or expansion fails to provide mechanical equilibrium of the tangential discontinuity downstream, developing an unstable solution with subsonic zones that grow with time (Martínez-Ruiz *et al.* 2019).

Considering that we will compare below the differences in reaction evolution between the shock-free base flow and the oblique shock impingement configurations, the post-shock conditions M_3, T_3 and M_4, T_4 are here matched to those of the free streams in the base-case mixing layer in absence of an incident shock wave ($M_1 = 2$, $T_1 = 1250$ K; $M_2 = 1.25$, $T_2 = 545$ K)$_{base}$. Figure 2(*b*) shows the locus of input parameters M_1, σ_i (circles) that produce the desired post-shock $M_3 = 2$ and corresponding M_2, σ_t (crosses) that warrants $M_4 = 1.25$ with a regular equilibrium solution. These conditions are used for the inlet of the impinging oblique shock simulations, together with new upstream values of T_1 and T_2 that provide the desired T_3 and T_4 once each shock intensity is known. Finally, it should be noted that the rightmost sets of solutions involve greater incident angles σ_i and Mach numbers of the free streams, which cause more intense reflected expansions that lower further the temperature and pressure of the final upper region 5. This cooling process – owing to the reflected rarefaction structure – is addressed in the following, where we will focus on its effect over the thermochemical problem.

For the sake of clarity, a first set of comparative simulations is presented in figure 3, whose numerical computation details are presented below. Figures 3(*a*,*c*) show a snapshot of the base-case reactive mixing layer (air–H_2) in a hot–cold configuration, once the ignition transient is produced. The instantaneous temperature (figures 3*a*,*b*) and numerical schlieren (figures 3*c*,*d*) distributions are presented to visualise the reactive layer and pressure wave structures, respectively. It should be noted that the sharp increase in temperature owing to the chemical reaction approximately indicates the characteristic ignition distance x_{ign}. Figures 3(*c*,*d*) depict the instantaneous pressure waves arising from the mixing layer and the reaction kernels, which are of acoustic type, $\Delta p \ll p \simeq 1$ atm.

Moreover, figures 3(*b*,*d*) show analogous distributions for the case with oblique shock impingement. The temperatures and Mach numbers of the incoming streams are selected to produce post-shock conditions that mimic the inlet in the shock-free reactive mixing layer. The ignition distance, given pre-shock mixing evolution and post-shock compressed conditions, is slightly reduced compared to the base case. In figure 3(*d*), the incident and transmitted shock waves are clearly detected as the most intense pressure gradient events,

https://doi.org/10.1017/jfm.2026.11936 Published online by Cambridge University Press

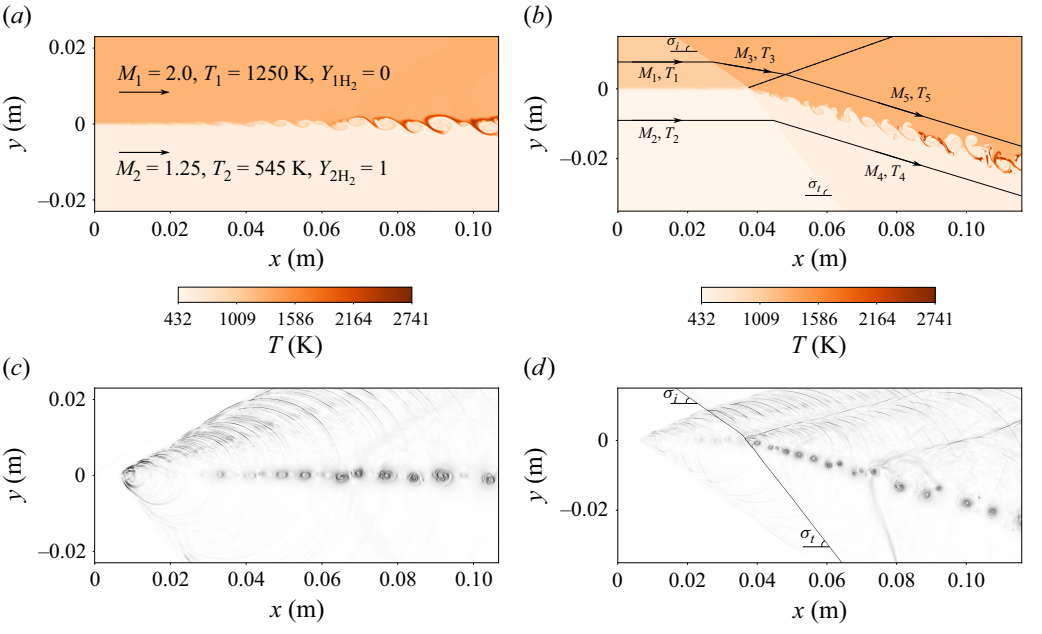


Figure 3. Mixing layer ignition (*a*,*c*) without and (*b*,*d*) with oblique shock impingement: (*a*,*b*) temperature and (*c*,*d*) numerical schlieren profiles. Inlet mixing layer profiles follow tanh-shape distributions.

$\Delta p \sim p$, including a reflected expansion of low intensity that cools down the upper stream. In turn, ignition- and vorticity-related acoustics can also be detected therein, starting at the point where a numerical forcing (vertical perturbation at $x \sim 0.01$ m) destabilises the layer. This disturbance physically displaces the shear layer, leading to local pressure fluctuations that propagate as acoustic waves.

These results enable the analysis of the isolated effects of ideal flow regular shock structures on the auto-ignition point and combustion dynamics. Nevertheless, the non-ideal effects and inner structure of the mixing layer are also of the greatest relevance, as the chemical reaction will take place wherever the reactants are heated up and mixed at a molecular level. For this reason, we will discuss in the following the prescribed profiles at the inlet of the numerical simulation domain.

2.2. *Inlet profiles*

The inlet values of each stream variable need to be provided through continuous profiles that represent a realistic upstream evolution of the diffusive processes. The domain is scaled with a characteristic vorticity thickness δ^0_ω, as depicted in figure 1. This thickness is a function of the distance to the virtual origin of the mixing layer, $x_0 = (\delta^0_\omega/2)^2 \rho_1 u_1/\mu_1$, with μ_1 the upper-stream viscosity, ρ_1 the density, and u_1 the free-stream speed. In turn, the vorticity Reynolds number is defined as

$$Re^0_\omega = \frac{\delta^0_\omega \bar{\rho}\, \Delta u}{\bar{\mu}}, \tag{2.1}$$

where $\Delta u = |u_1 - u_2|$, $\bar{\rho} = (\rho_1 + \rho_2)/2$ and $\bar{\mu} = (\mu_1 + \mu_2)/2$. Following previous works (Rogers & Moser 1994), the vorticity Reynolds number is set to $Re^0_\omega = 3200$, which defines the inlet vorticity thickness of the layer δ^0_ω. In addition, to induce Kelvin–Helmholtz

https://doi.org/10.1017/jfm.2026.11936 Published online by Cambridge University Press

instabilities, the aforementioned random perturbation is applied to the transverse velocity component v at $(x,\ y) = (4\delta^0_\omega,\ 0)$.

Most common input distributions of flow variables in mixing-layer and shear-layer numerical studies involve hyperbolic tangent profiles, as a smooth characteristic transverse evolution of generic fluid variables,

$$\Phi = \frac{\Phi_1 + \Phi_2}{2} + \frac{\Phi_1 - \Phi_2}{2} \tanh\left(\frac{2y}{\delta^0_\omega}\right), \tag{2.2}$$

which is typically used for the streamwise velocity, temperature, and species. Other subsidiary magnitudes such as the Mach number can be obtained given the isobaric co-flow composition Y_i. Nevertheless, a self-similar solution can be predicted owing to the lack of characteristic length in mixing-layer configurations. In fact, Huete *et al.* (2016) showed that the self-similar solution of a laminar mixing layer can be calculated – Soret and Dufour effects included – as a function of the dimensionless similarity coordinate $\eta = y/[(\mu_1/\rho_1)x/u_1]^{1/2}$. The dimensionless longitudinal velocity component $U(\eta) = u/u_1$, and transverse velocity component $V(\eta) = v/u_1$, temperature $\Theta(\eta) = T/T_1$ and density $R(\eta) = \rho/\rho_1$, are referred to the characteristic upstream values. Then the calculation of the self-similar profiles is performed with non-negligible Rayleigh viscous dissipation and temperature-dependent transport coefficients.

Consequently, the dimensionless mass, momentum, energy and species conservation equations for the self-similar problem can be written as

$$-\frac{\eta}{2}\frac{\mathrm{d}}{\mathrm{d}\eta}(RU) + \frac{\mathrm{d}}{\mathrm{d}\eta}(RV) = 0, \tag{2.3}$$

$$R\left(V - \frac{\eta}{2}\right)\frac{\mathrm{d}U}{\mathrm{d}\eta} = \frac{\mathrm{d}}{\mathrm{d}\eta}\left(\mathcal{M}\frac{\mathrm{d}U}{\mathrm{d}\eta}\right), \tag{2.4}$$

$$\begin{aligned} RC_p\left(V - \frac{\eta}{2}U\right)\frac{\mathrm{d}\Theta}{\mathrm{d}\eta} = {} & \frac{\mathrm{d}}{\mathrm{d}\eta}\left(\frac{\mathcal{M}C_p}{Pr}\frac{\mathrm{d}\Theta}{\mathrm{d}\eta}\right) - \left(\mathcal{W}_2^{-1} - 1\right)J\frac{\mathrm{d}\Theta}{\mathrm{d}\eta} \\ & - \frac{\alpha\,(\gamma-1)}{\mathcal{W}_2\gamma}\frac{\mathrm{d}}{\mathrm{d}\eta}\left(\mathcal{W}J\Theta\right) + (\gamma-1)\,M_1^2\mathcal{M}\left(\frac{\mathrm{d}U}{\mathrm{d}\eta}\right)^2, \end{aligned} \tag{2.5}$$

$$R\left(V - \frac{\eta}{2}U\right)\frac{\mathrm{d}Y}{\mathrm{d}\eta} = -\frac{\mathrm{d}J}{\mathrm{d}\eta}, \tag{2.6}$$

where the local composition is defined in terms of the mass fraction of fuel Y. Here, $C_p = c_p/c_{p1}$ is the dimensionless specific heat at constant pressure, $\mathcal{M} = \mu/\mu_1$ is the dimensionless viscous coefficient, γ is the adiabatic index, and $\alpha = -0.3$ is the thermal-diffusion factor, considered constant. The Prandtl number is also taken constant and equal to $Pr = \mu c_p/\lambda = 0.7$, where λ stands for thermal conductivity. In addition, $\mathcal{W} = W/W_1$, where W refers to mixture molecular weights, and $\mathcal{W}_2 = W_2/W_1$. Finally, J is the fuel-diffusion flux non-dimensionalised with $\rho_1\mu_1u_1/x$, and obtained explicitly from Sánchez & Williams (2014):

$$J = -\frac{R\mathcal{D}}{Pr\ Le}\left(\frac{\mathrm{d}Y}{\mathrm{d}\eta} + \alpha\frac{Y(1-Y)}{\Theta}\frac{\mathrm{d}\Theta}{\mathrm{d}\eta}\right), \tag{2.7}$$

https://doi.org/10.1017/jfm.2026.11936 Published online by Cambridge University Press

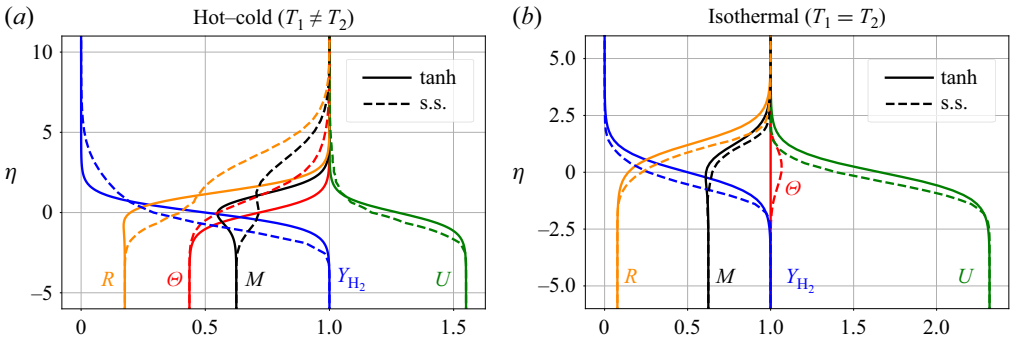


Figure 4. Comparison between hyperbolic tangent (tanh) profiles (solid) and self-similar (s.s.) profiles (dashed) for (*a*) hot–cold and (*b*) isothermal H_2–air mixing layers.

where $\mathcal{D} = D/D_1$ is the dimensionless binary diffusion coefficient. The system of equations must be completed with the equation of state

$$RT = \mathcal{W} = \frac{1}{1 + \left(\mathcal{W}_2^{-1} - 1\right)Y}, \tag{2.8}$$

and the expressions

$$\mathcal{M} = \frac{1 + [(\mu_2/\mu_1)\mathcal{W}_2^{-1/2} - 1]Y}{1 + (\mathcal{W}_2^{-1/2} - 1)Y} T^{\sigma_1}, \quad \mathcal{D} = T^{1+\sigma_1} \quad \text{and} \quad C_p = [1 + (\mathcal{W}_2^{-1} - 1)Y]T^{\sigma_2} \tag{2.9}$$

for the variations of the transport coefficients and specific heat with temperature and composition, taking the values $\sigma_1 = 0.7$ and $\sigma_2 = 0.2$ (Rosner 2012).

Numerical integration of the system of equations between the far-field conditions of streams 1 and 2 yields the profiles of flow variables across the self-similar laminar mixing layer. Figure 4 depicts the difference between the hyperbolic tangent (solid) and self-similar (dashed) profiles obtained for the same simulation inputs in hot–cold scenarios and isothermal co-flow. Both the hyperbolic tangent and self-similar profiles are initialised with the same vorticity thickness δ_ω^0, ensuring that they start from an equivalent large-scale mixing condition.

The main intention of the comparison is to assess that ignition is sensitive not only to bulk parameters (e.g. vorticity thickness or global stream conditions), but also to the detailed thermochemical state contained in the profile structure. It should be noted that the widely used hyperbolic tangent is not representative of the particular thermal and mass diffusive processes of H_2–air mixtures, where its characteristic diffusivity and disparate stream densities are playing an important role in the development of the inner region of the mixing layer. In fact, several effects should be highlighted here, such as the density gradient, the non-symmetric shift of temperature, and the non-monotonic Mach number distribution (figure 4*a*), or the temperature increase through viscous dissipation in the isothermal case (figure 4*b*), with major local variations inside the mixing-layer thickness $\eta \sim O(1)$. The effect of the input profile on the ignition distance is also compared in the following sections, showing the great relevance of including detailed physical processes at the inlet of the domain.

https://doi.org/10.1017/jfm.2026.11936 Published online by Cambridge University Press

3. Numerical set-up

The two-dimensional DNS results presented below were performed with CREAMS (compressible reactive multi-species solver), that makes use of a third-order Runge–Kutta time integration scheme. In the spatial discretisation it employs a WENO scheme with seventh-order accuracy, while the viscous and diffusive terms, on the other hand, are solved with an eighth-order centred finite-difference scheme. The solver CREAMS has been extensively verified and validated in prior work by Martínez-Ferrer *et al.* (2014), a study that provides a comprehensive assessment of the numerical schemes and physical models, including benchmarks such as shock tubes, advection–diffusion problems, premixed flames, reactive jets, and shock–mixing-layer interactions, demonstrating the solver's accuracy for compressible reacting flows. Additionally, CREAMS has been used in other studies involving supersonic mixing layers, inert and reactive (Ferrer *et al.* 2012; Techer *et al.* 2015).

Ignition characteristics in hydrogen–air systems can exhibit some sensitivity to the choice of kinetic mechanism, particularly in terms of ignition delay. However, as the focus of the present study is on the relative influence of flow configuration and inlet thermochemical structure, rather than on absolute ignition timing, the detailed H_2–air San Diego mechanism updated by Sánchez & Williams (2014), with 20 steps and 9 species, is selected without including any sensitivity analysis. This reaction mechanism is a well-established and widely validated kinetic model for hydrogen combustion, known to provide accurate predictions of ignition and flame behaviour over a broad range of conditions.

The layers are initialised with an inert flow field, and integrated in time until a statistically steady state of reacting flow is achieved. Nevertheless, we will consider that the chemical reactions occur rapidly, the reactive characteristic time being much shorter than the convective and diffusive ones. This separation of scales enables CREAMS to use the second-order Strang splitting method, which isolates the treatment of the chemical source terms from the rest of the problem. The method integrates in a first step the non-reactive part of the Navier–Stokes equations for a multi-species flow, convection and diffusion terms, and the reaction rates over a steady flow are allowed to evolve during a second step (Strang 1968). The unsteady problem is thus modelled as

$$\frac{\partial Q}{\partial t} + \frac{\partial F_j}{\partial x_j} = \frac{\partial G_j}{\partial x_j} + S, \tag{3.1}$$

with the vector of conservative variables Q, the convective flux F_j, the diffusive flux G_j, and the chemical source term S.

The Strang splitting method separates the operators of the inert terms L_i, namely

$$\frac{\partial Q}{\partial t} = L_i(Q(t)) = -\frac{\partial F_j}{\partial x_j} + \frac{\partial G_j}{\partial x_j}, \tag{3.2}$$

and the reactive terms L_r,

$$\frac{\partial Q}{\partial t} = L_r(Q(t)) = S. \tag{3.3}$$

The integration of the inert terms equations is performed with a Runge–Kutta total variation diminishing scheme of third order in the following steps. First, (3.3) is integrated with previous conditions with a time step $\Delta t/2$, which is then used to integrate the inert system of (3.2) over a time step Δt. Finally, this intermediate solution is used to integrate again the reactive set in (3.3) for another half-step $\Delta t/2$.

The boundary conditions at the inlet prescribe upstream properties and profiles as presented in § 2.2. The remaining boundaries of the simulation domain are all set

https://doi.org/10.1017/jfm.2026.11936 Published online by Cambridge University Press

as supersonic outputs, with a coarse-mesh 'foam' zone at the right-hand side outlet to mitigate acoustic reflections. The domain rectangular mesh is systematically scaled with the selected inlet vorticity thickness. The size of the domain $L_x \times L_y$ is modified depending on the scenario to adequately capture the geometric distribution and possible flow deflection, with $[L_x/\delta^0_\omega, L_y/\delta^0_\omega] = [400, 100]$ in absence of an oblique shock, and $[L_x/\delta^0_\omega, L_y/\delta^0_\omega] = [210, 550]$ in the presence of an impinging shock. A rectilinear structured mesh of characteristic cell size $\Delta x/\delta^0_\omega = 0.03$ is employed at the most relevant region, bounded to the inlet and centred on the mixing layer, with sizes $[L'_x/\delta^0_\omega, L'_y/\delta^0_\omega] = [360, 60]$ in the base cases, and a shock-angle-dependent domain $[L'_x/\delta^0_\omega, L'_y/\delta^0_\omega] = [150, 2d_{imp}\tan(\sigma_i)]$ otherwise, rescaled with the shock impingement distance from the inlet d_{imp}. Then a progressive coarsening of the mesh is selected towards the outlet boundaries (top, bottom and right). In order to reduce the computational cost of the simulations, the chemical reaction is not computed in the far-field regions of the coarse mesh. The resolution criterion considered in the study was based on the computation of the laminar flame thickness δ_L, which can be considered as the most restrictive scale in the reacting mixing layer. The flame thickness is evaluated from the computation of one-dimensional counter-flow flames at the conditions of the mixing layer (performed using Cantera) across the stable branch of the S-curve. From the different values obtained, the minimum flame thickness, defined as the ratio of the total temperature rise to the maximum temperature gradient, is selected. The grid spacing is chosen such that at least 15 grid points are used to resolve the flame thickness for the minimum flame thickness, in line with established DNS resolution criteria for reacting flows (Dinesh *et al.* 2016; Klein *et al.* 2020). This criterion ensures that the most restrictive reacting scales are adequately resolved in all cases, for both shock-free and shock-assisted configurations. While a strict Kolmogorov scale estimate is not directly applicable in the present compressible, transitional mixing-layer configuration, the chosen resolution ensures that both the velocity and scalar gradients are adequately resolved without the need for subgrid-scale modelling.

Finally, the time step varies for each case study. It is obtained through the cell size Δx, the local speed of sound c, and the Courant–Friedrichs–Lewy number (CFL) fixed at 0.5, according to

$$\Delta t = \frac{CFL}{\max[(|u(x, y)| + c(x, y))/\Delta x, (|v(x, y)| + c(x, y))/\Delta y]}. \tag{3.4}$$

All simulations (see table 1) were performed on the general partition of the MareNostrum 5 system based on Intel Sapphire Rapids processors (4th generation Intel Xeon scalable processors). The computational cost varies depending on the flow configuration (reacting versus non-reacting, with or without shock wave). Mixing-layer simulations without shock wave (hot–cold case) take approximately 36 064 core-hours (23 h on 1568 cores) for a single residence time without chemical reactions. When chemical reactions are included, one residence time requires approximately 68 208 core-hours (43.5 h on 1568 cores). The full simulation consists of an initial inert development phase followed by a reacting phase lasting approximately 3.7 residence times, leading to a total computational cost of approximately 288 434 core-hours. However, isothermal cases without shock wave impose lower computational cost due to the reduced stiffness. A non-reacting residence time requires approximately 8064 core-hours (6 hours on 1344 cores), while a reacting residence time requires approximately 17 472 core-hours (13 h on 1344 cores). The total cost for a complete simulation is approximately 72 710 core-hours.

https://doi.org/10.1017/jfm.2026.11936 Published online by Cambridge University Press

Base case		M_1	M_2	$T_1\,(K)$	$T_2\,(K)$		Inlet profiles
1		2	1.25	1250	545		(a) tanh, (b) self-similar
2		2	1.25	1250	1250		(a) tanh, (b) self-similar
Case	σ_i (deg.)	M_3	M_4	$T_3\,(K)$	$T_4\,(K)$	$d_{imp}\,(\delta^0_\omega)$	Inlet profiles
3	32.5	2	1.25	1250	545	50	(a) tanh, (b) self-similar
4	35.0	2	1.25	1250	545	50	(a) tanh, (b) self-similar
5	37.5	2	1.25	1250	545	50	(a) tanh, (b) self-similar
6	40.0	2	1.25	1250	545	50	(a) tanh, (b) self-similar
7	35.0	2	1.25	1250	545	20	(a) tanh, (b) self-similar
8	35.0	2	1.25	1250	545	70	(a) tanh, (b) self-similar

Table 1. Base case of supersonic reactive mixing layers of H_2–air without impinging shock (cases 1 and 2) and incident oblique shock wave cases of supersonic reactive mixing layer (cases 3–8).

Finally, mixing-layer simulations with shock waves were performed using 2688 cores. The total computational cost depends on the shock inclination angle owing to the mesh distribution: cases with $\sigma_i = 32.5°$ are completed in 70 114 core-hours; cases with $\sigma_i = 35.0°$ take 106 123 core-hours; and cases with $\sigma_i = 37.5°$ require 105 322 core-hours.

In the next section, a thorough analysis of the supersonic reactive mixing-layer features is presented. In particular, the auto-ignition process is addressed, highlighting the interpretation of the intervening physical mechanisms.

4. Auto-ignition of shock-free supersonic mixing layers

The auto-ignition of supersonic mixing layers presented here includes various simulation cases gathered in table 1. The configurations without oblique shock impingement (cases 1 and 2) are first presented as reference cases to provide further understanding on the effect of boundary conditions, both in each far-field stream and in the variable profiles stated at the inlet. Thereafter, § 5 will analyse the effect of the shock-wave impingement on the mixing layer, isolating its influence by ensuring that the post-shock conditions are identical to those of the reference cases presented here.

4.1. *General features of shock-free mixing layers*

The temperature distributions of the base set of simulations, cases 1 and 2, are presented in figure 5 after 3.7 residence times, when the statistically steady flow is already established. The panels offer a comparison of the different macroscopic flow features between the classical hyperbolic tangent inlet (figures 5*a*,*c*) and the self-similar profiles (*d*) for the hot–cold (figures 5*a*,*b*) and isothermal (figures 5*c*,*d*) supersonic mixing layers. The first appreciative difference between the cases is the average thickness and vorticity scales appearing in the flow structure. This differential behaviour is controlled by stronger inertial effects at the fuel-side edge ($y < 0$) of the self-similar case, where a larger density value is prescribed through incorporation of adequate mixing mechanisms (see discussion above). These changes produce a greater penetration of the vortical structures in the lower cold stream of figure 5(*b*) than in the tanh case of figure 5(*a*). In turn, the greater spread of reactant in the self-similar input also contributes to thicker reaction layers upon the ignition event. In the isothermal co-flow case 2 in figure 5(*d*), the temperature increase produced by the viscous dissipation mechanism brings the ignition event forward compared to the tanh

https://doi.org/10.1017/jfm.2026.11936 Published online by Cambridge University Press

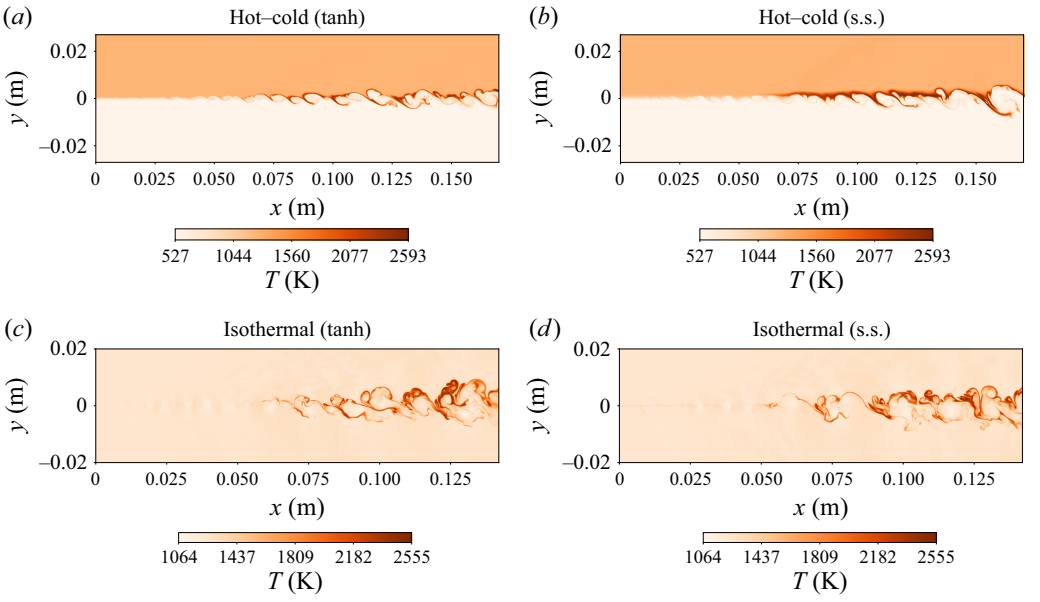


Figure 5. Temperature distributions of (*a*,*b*) hot–cold and (*c*,*d*) isothermal reactive mixing layers, with (*a*,*c*) tanh and (*b*,*d*) self-similar inlet profiles.

case in figure 5(*c*), by approximately 15 % of the distance to the inlet of the computational domain.

In fact, these particular effects are quantified in figure 6, where the evolution of the vorticity thickness δ_ω along the mixing layer is shown. The thickness value is computed as

$$\delta_\omega = \frac{U_1 - U_2}{|\partial \langle u_1 \rangle_f / \partial y|_{max}}, \tag{4.1}$$

where the operator $\langle \bullet \rangle_f = \langle \rho \bullet \rangle / \langle \rho \rangle$ stands for Favre average. The growth of δ_ω differs slightly in the hot–cold scenario in figure 6(*a*), with large differences in the transverse distributions of variables as prescribed by the inlets (presented in figure 4*a*). Nevertheless, the isothermal results in figure 6(*b*) show a nearly identical evolution, with initial distributions that bear a greater resemblance (recall the profiles compared in figure 4*b*).

Therefore, a first outcome of the present work on the comparison of inlet profiles is that the incorporation of major differences in density and momentum distributions, owing to diffusive mixing of hydrogen, does indeed affect the shape and size of the flow field, yet it barely modifies the time-averaged ignition distance marked in figure 6(*a*), given that the maximum injection temperature remains unaffected. Contrarily, when the thermal viscous dissipation effect is dominant in the isothermal case and is included via the self-similar inlet profile (figure 6*b*), the reaction is enhanced and brought forward without great influence on the flow field or vorticity thickness scale.

To obtain the value of the ignition distance d_{ign}, a clear and unambiguous criterion of the ignition event is defined, ruling out popular temperature-increase criteria, which could be triggered here due to the aforementioned friction heating of supersonic shear layers with no relevant initiation of the chemical reaction. First, several alternative variables are considered to obtain the coordinates of the auto-ignition point, by namely the production rates of some of the radical species that control the chemical reaction $\dot{\omega}_H$, $\dot{\omega}_O$ and $\dot{\omega}_{OH}$. Moreover, it was shown by Sánchez *et al.* (2012) that the ignition

https://doi.org/10.1017/jfm.2026.11936 Published online by Cambridge University Press

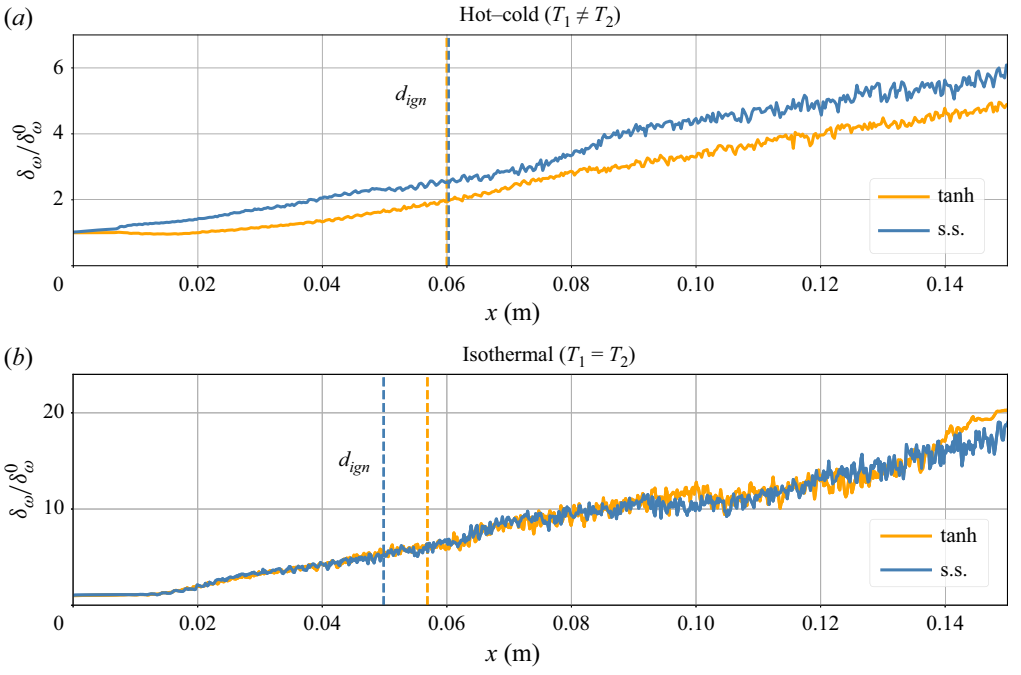


Figure 6. Spatial evolution of the time-averaged vorticity thickness δ_ω with respect to the inlet-profile thickness in the base mixing layers, for (*a*) case 1 and (*b*) case 2. Ignition distances are marked with vertical dashed lines.

process of hydrogen combustion was indeed controlled by the particular combination of radicals production–consumption rates $\dot{\omega}_m = \dot{\omega}_H + 2\dot{\omega}_O + \dot{\omega}_{OH}$. Therefore, to calculate the instantaneous auto-ignition point for a given simulation case, we first evaluate the iso-contour of the composite reaction-rate value $\dot{\omega}_m$ that sits above a selected percentile level (99.9 %), and then compute its nearest point to the inlet. The percentile threshold used to define the ignition point was selected after examining a range of high-percentile values. It was observed that the ignition distance converged to the same values for sufficiently high thresholds, and that values above 99.9 % (e.g. 99.95 %) tended to capture isolated, non-representative peaks that appear downstream and do not correspond to the primary ignition event. Therefore, the 99.9 % level was chosen as a compromise between robustness and physical relevance. As this position can vary for each time step of the simulation, the ignition distance d_{ign} is averaged over the statistically steady temporal span, which is approximately 3.7 characteristic residence times of the numerical domain.

Figures 7(*a*,*b*) show the values of the most x-advanced position of the reaction-rate criteria for increasing percentiles (nearly maximum values) based on different radical reaction rates. Note that all the criteria explored herein converge for sufficiently high percentiles, and that the maxima are avoided owing to singularities and outliers that can appear in diverse reactive kernels far downstream from the auto-ignition event. Additionally, the comparison of the results for different inlet profiles is offered for hyperbolic tangent (solid) and self-similar (dashed) inlet cases. The results for hot–cold layers in figure 7(*a*) show that the ignition distance for the 99.9 % level is nearly 6 cm and does not vary for the different input profiles. However, the ignition position above the mixing-layer centreline y_{ign} shown in figure 7(*c*) is doubled for the self-similar inlet condition, pointing at the greater relevance of realistic reactant mixing, and

https://doi.org/10.1017/jfm.2026.11936 Published online by Cambridge University Press

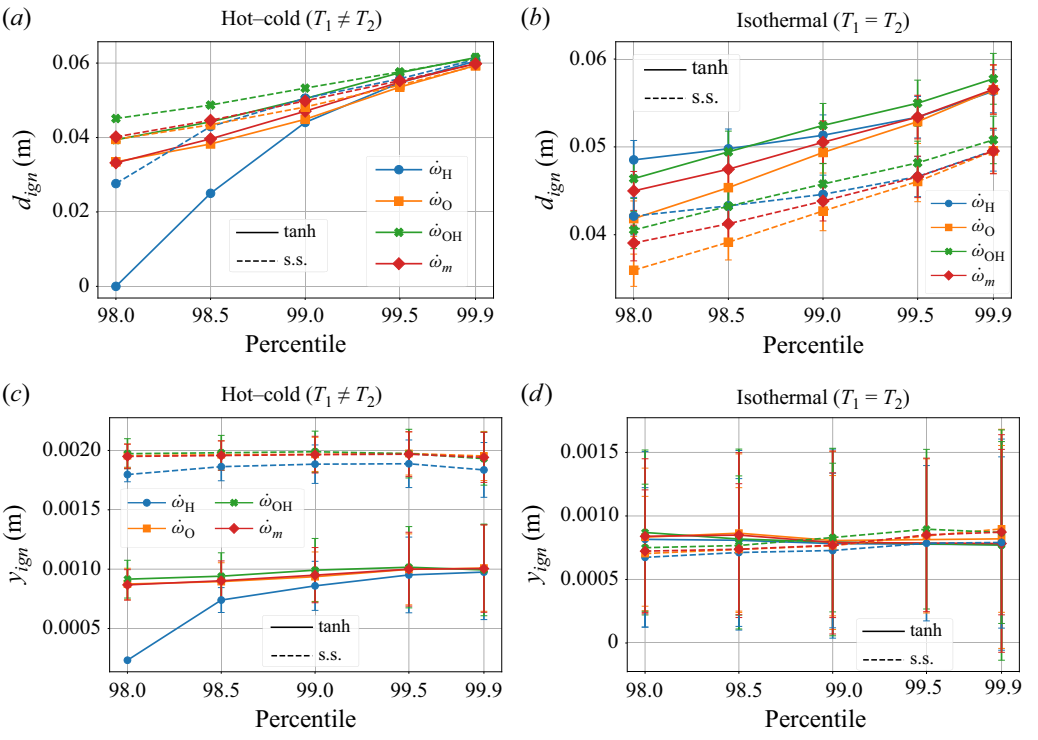


Figure 7. Auto-ignition averaged (*a,b*) distance d_{ign} and (*c,d*) vertical coordinate y_{ign}, for different production-rate criteria $\dot{\omega}_i$, in the (*a,c*) hot–cold and (*b,d*) isothermal cases.

probably indicating that the unchanged ignition distance is thermally controlled in this configuration, as predicted by Treviño & Liñán (1995). Our results support the asymptotic analyses of Treviño & Liñán (1995) for self-ignition in the simplest iso-velocity mixing-layer configuration. Specifically, when the temperature difference between streams is sufficiently large, the ignition location is controlled mainly by thermal diffusion and chemical induction, whereas moderate velocity variations play only a minor role. A similar conclusion applies in the opposite limit of fully developed turbulent mixing layers. The analysis of Im *et al.* (1998) shows that at sufficiently high temperatures, ignition is determined primarily by the interplay between chemical induction and scalar mixing time scales. In this regime, turbulence mainly affects the spatial distribution and intermittency of ignition kernels, while having only a limited impact on the overall ignition delay under the conditions considered.

On the other side, isothermal configurations show a reduction of the auto-ignition distance in figure 7(*b*) while the vertical position of the ignition point is unaffected by the type of inlet profile in figure 7(*d*). This fact was previously attributed to the friction-related temperature increase in the self-similar inlet condition with detailed mechanisms. Moreover, these preheated-fuel isothermal layers show a consistent reduction of the ignition distance when compared to the hot–cold cases of approximately 0.2 cm, and a further reduction of more than 1 cm in the self-similar case, with the initial extra temperature bump owing to thermal viscous dissipation. The approximately 50 K temperature rise generated in the self-similar case, superimposed on the 1250 K

https://doi.org/10.1017/jfm.2026.11936 Published online by Cambridge University Press

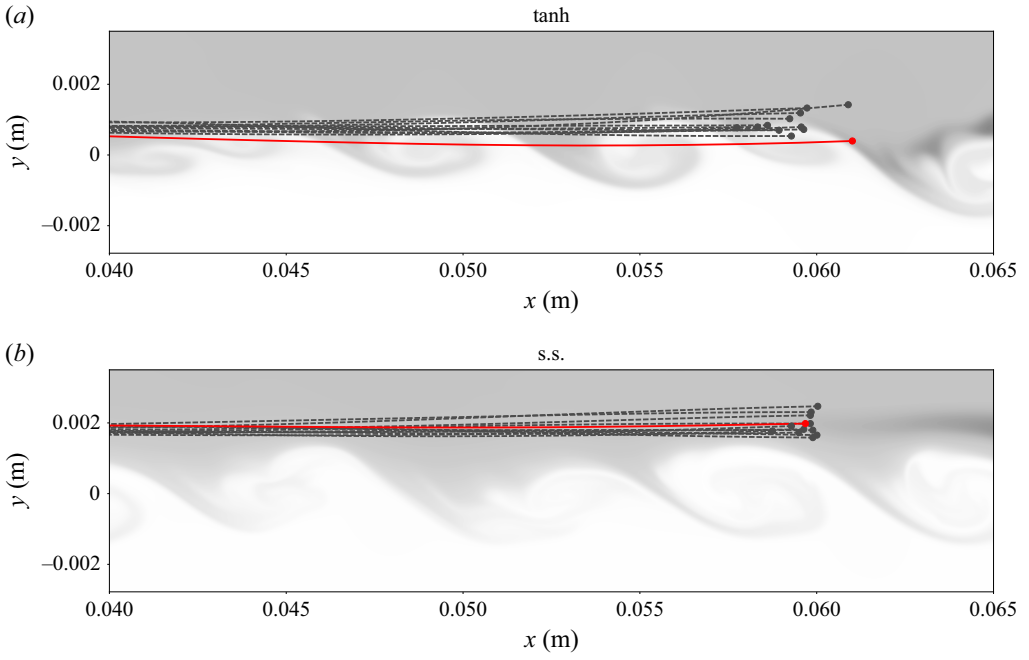


Figure 8. Case 1 temperature fields and superimposed pathlines of fluid particles used to detect auto-ignition, for (*a*) tanh and (*b*) self-similar inlet conditions.

outer-stream temperature and absent from the prescribed inlet conditions of the hyperbolic-profile case, results in an approximately 25 % reduction in ignition distance. This decrease is broadly consistent with the reduction in homogeneous auto-ignition time reported in Sánchez & Williams (2014).

This behaviour differs from both the iso-velocity configuration examined in Treviño & Liñán (1995) and the turbulent configuration investigated in Im *et al.* (1998). Accordingly, an important conclusion of this subsection is that velocity gradients, when viscous dissipation is consistently accounted for, generate non-negligible temperature fluctuations that fundamentally alter the ignition dynamics of externally isothermal configurations. Moreover, beyond their impact on ignition analyses based on homogeneous assumptions and the associated reduction in ignition delay times, these effects also alter scalar transport by the Soret effect, thereby contributing further to the reduction in ignition distance. Additional details are provided below.

4.2. *Specific results for non-isothermal streams*

The ignition mechanism for case 1, involving $T_1 = 1250$ K and $T_2 = 545$ K, is analysed in figure 8 with the detailed comparison between the tanh (figure 8*a*) and self-similar (figure 8*b*) inlet profiles. The two-dimensional temperature field distribution at $t = 0.0006$ s is presented with superimposed trajectories, for the fluid particle that is detected as the most-advanced ignition point at different instants. Each pathline, showing the history of the evolving fluid particle, is integrated backwards from the detected ignition spot using the stored velocity fields from the whole simulation. The detected igniting particle at $t = 0.0006$ s is shown in red.

First, we point out that the temporal dispersion of detected pathlines, in both inlet subcases, is small. Moreover, the ignition points are also contained in a well defined

https://doi.org/10.1017/jfm.2026.11936 Published online by Cambridge University Press

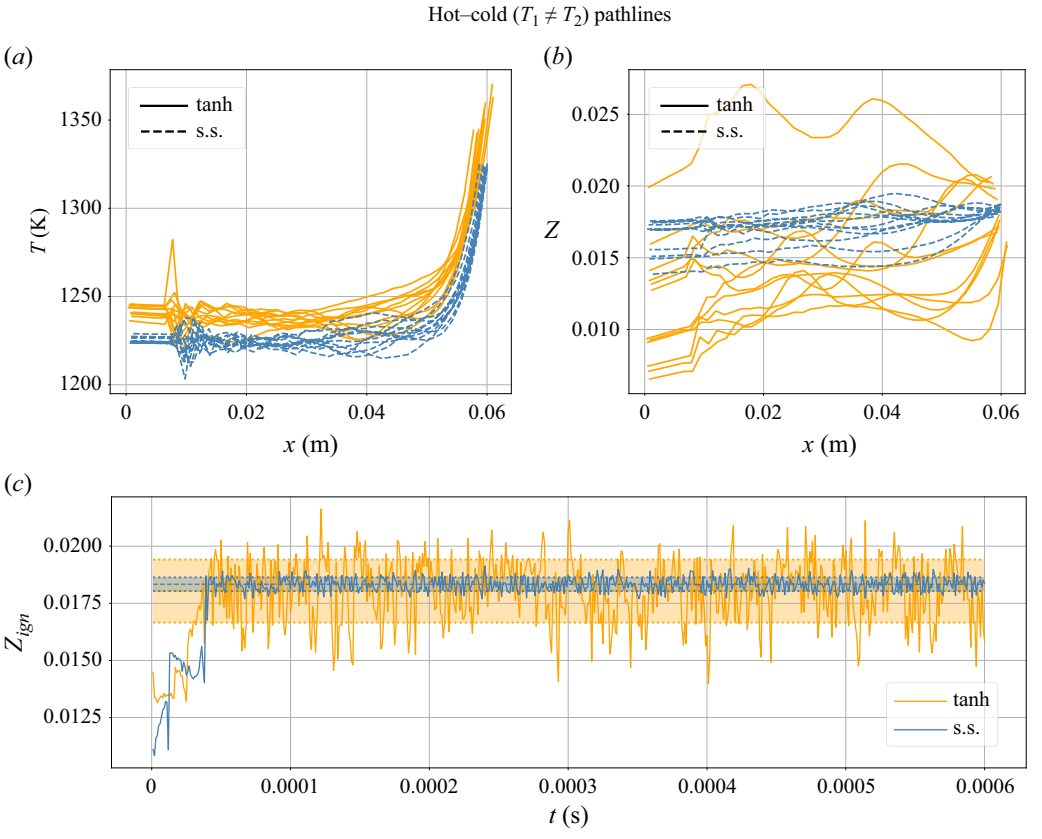


Figure 9. Case 1 (*a*) temperature and (*b*) mixture fraction variation along the pathlines. (*c*) Time evolution of the mixture fraction value at the auto-ignition point Z_{ign}.

ignition distance. However, the nature of the ignition on the self-similar condition shows in figure 8(*b*) a clear shift towards the hot-side stream, which can be explained by comparing the inlet profiles of figure 4(*a*): greater y-coordinate positions are required to find high temperature values, and in turn sit on larger amounts of fuel owing to the consideration of realistic mass diffusion. This temperature-controlled shifting behaviour is hindered by the smaller mixing thickness in the hyperbolic tangent case in figure 8(*a*), which can be traced above in figure 6(*a*), and as a result, the igniting fluid parcels follow paths well contained in the roller region.

The nature of each auto-ignition regime can be explored through the information presented in figure 9. First, the temperature T evolution over each detected ignited flow particle trajectory (figure 9*a*) shows a coherent build-up with the reaction initiation, which starts from slightly hotter conditions in the hyperbolic tangent case. However, the mixture fraction Z evolution along the pathlines (figure 9*b*) shows a very different behaviour in each scenario. The mixture fraction definition used here is

$$Z = \frac{S\hat{Y}_{H_2} - \hat{Y}_{O_2} + 1}{S + 1}, \tag{4.2}$$

where $\hat{Y}_{H_2}$ and $\hat{Y}_{O_2}$ are normalised values of the fuel and oxidiser mass fractions, referred to upstream values of the bottom and top streams, respectively:

https://doi.org/10.1017/jfm.2026.11936 Published online by Cambridge University Press

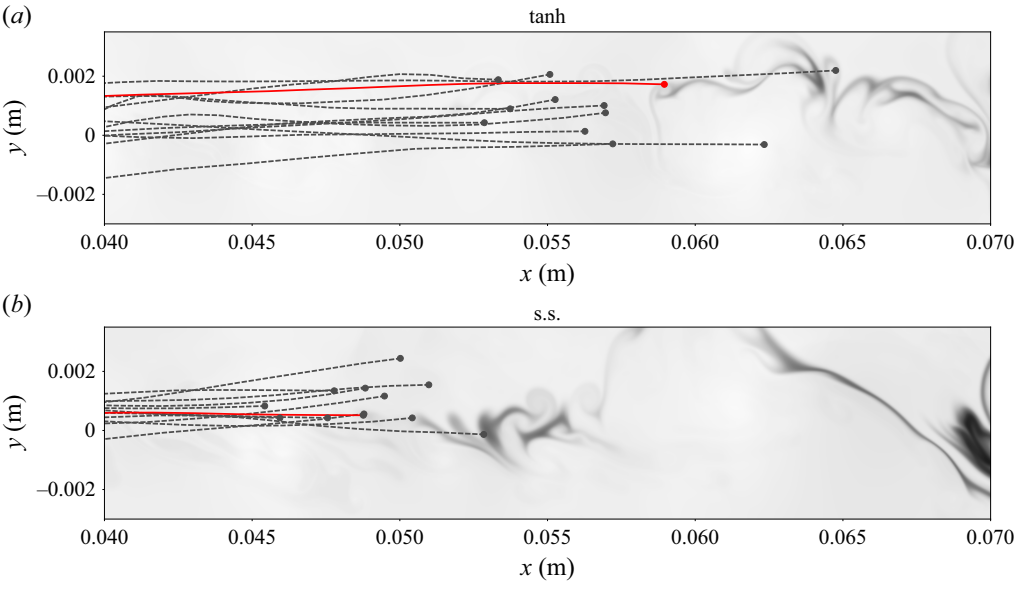


Figure 10. Case 2 temperature field and ignition pathlines for different inlet conditions.

$$\hat{Y}_{H_2} = \frac{Y_{\mathrm{H}_2}}{Y_{\mathrm{H}_2,0}\big|_2}, \quad \hat{Y}_{\mathrm{O}_2} = \frac{Y_{\mathrm{O}_2}}{Y_{\mathrm{O}_2,0}\big|_1}, \quad S = \frac{sY_{\mathrm{H}_2,0}\big|_2}{Y_{\mathrm{O}_2,0}\big|_1}. \tag{4.3}$$

In particular, $s = 8$ is the amount of oxygen consumed per unit mass of hydrogen burnt, and the mass fractions for vitiated air $Y_{\mathrm{O}_2} = 0.2448$, $Y_{\mathrm{N}_2} = 0.5799$ and $Y_{\mathrm{H}_2O} = 0.1748$ that correspond to the molar fractions $X_{\mathrm{O}_2} = 0.201$, $X_{\mathrm{N}_2} = 0.544$ and $X_{\mathrm{H}_2O} = 0.255$. Therefore, $S = 32.68$ and the stoichiometric value of the mixture fraction is $Z_{st} = 1/(S+1) \simeq 0.0297$, considerably higher (+50 %) than the values found at the detected ignition Z_{ign} displayed along time in figure 9(*c*). It should be noted that the standard deviation of the mixture fraction value (shaded regions) is much larger for the hyperbolic tangent inlet, where the relevant thermochemical region sits in the central part of the unstable shear layer, strongly entangled with the roller motion.

4.3. *Specific results for isothermal streams*

The shock-free case 2 is conformed by a co-flow of air and fuel at the same temperature $T_1 = T_2 = 1250$ K. The results show a much larger spatial dispersion of the igniting particles paths, given that the hot region is not constrained to one side of the layer. The self-similar case in figure 10(*b*), including a viscous-dissipation temperature increase (see figure 4*b*), provides shorter ignition distances than the hyperbolic tangent condition in figure 10(*a*), as already stated above. On top of that, the pre-heated hydrogen stream promotes even higher density and velocity changes across the layer for the same outer-region Mach numbers M_1 and M_2 compared to the hot–cold configuration of case 1. This fact enhances the hydrodynamic destabilisation of the shear layer, thus promoting the formation of intense vortical structures.

The temperature evolution over the trajectories plotted in figure 11(*a*) shows a much larger irregularity than case 1 solutions, with localised temperature decrease below 1250 K owing to the dynamics of the shear-vortex layer and its non-negligible local expansion. In turn, the disparity in flow-particle history renders a wide range of Z values (from

https://doi.org/10.1017/jfm.2026.11936 Published online by Cambridge University Press

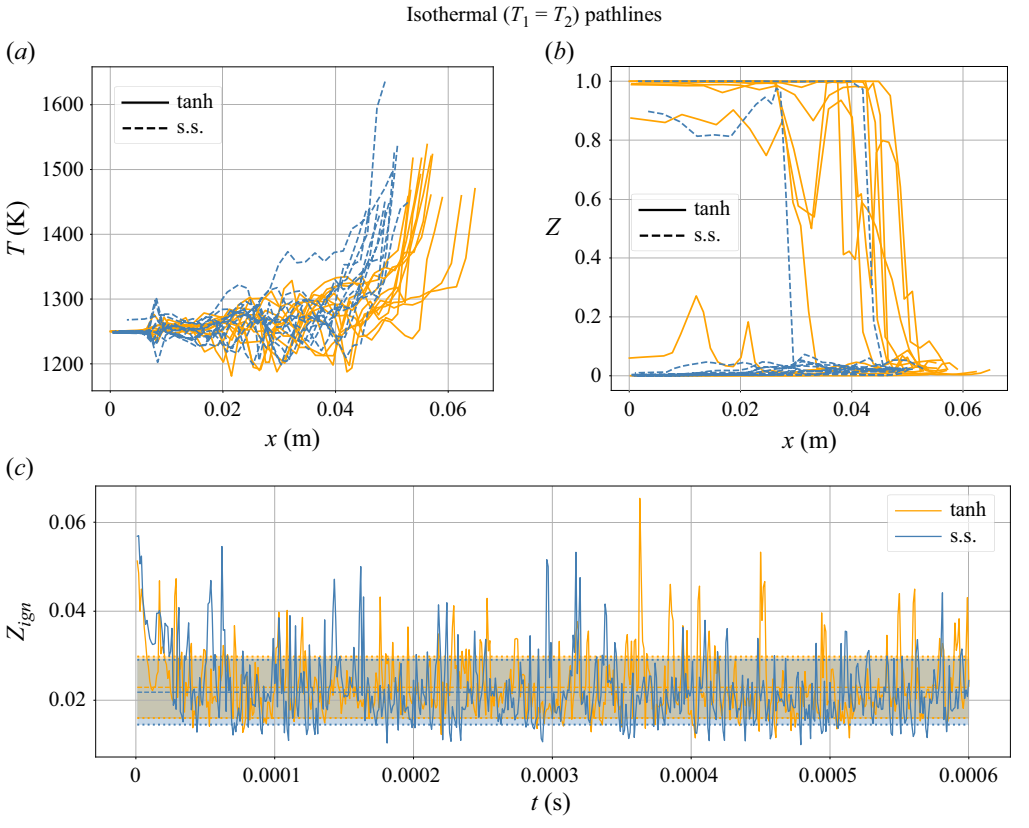


Figure 11. Case 2 (*a*) temperature and (*b*) mixture fraction variation along the pathlines. (*c*) Time evolution of the mixture fraction value at the auto-ignition point Z_{ign}.

0 to 1) at the origin of the ignition-detection pathlines shown in figure 11(*b*), along which mixing must also build up fast. Finally, figure 11(*c*) allows us to identify an equally disperse Z_{ign} oscillation in time for both inlet conditions. Unlike what was observed in figure 9 associated with non-isothermal streams, the standard deviation of the mixture fraction value (shaded regions) is barely affected by the choice of the inlet profile. As a result, it seems that the relevance of the inlet-profile information in a highly disturbed hydrodynamic configuration is primarily lost, showing very comparable trends in terms of auto-ignition character variability for both hyperbolic tangent and self-similar cases.

However, we should highlight the two key competing effects from the upstream boundary condition: (i) inertia variations driven by advanced description of temperature and composition of the co-flow mixing layer, and (ii) temperature increase owing to thermal viscous dissipation that accelerates the initiation of chemical reactions. From the results analysed herein, the former seems to promote homogenisation through flow destabilisation, while the latter acts strongly to reduce the ignition distance d_{ign}.

5. Auto-ignition of shock-assisted supersonic mixing layers

The streams selected for the case studies with oblique shocks are here defined by temperatures and Mach numbers that make the post-shock conditions match the values used in the non-isothermal base case 1 ($M_3 = 2.0$, $T_3 = 1250$ K; $M_4 = 1.25$, $T_4 = 545$ K).

https://doi.org/10.1017/jfm.2026.11936 Published online by Cambridge University Press

The purpose is to isolate the influence of shock-induced flow structures on the ignition process, independently of the well-known thermodynamic effects of temperature and pressure increases across the shock. The canonical configuration is designed to separate competing mechanisms and enable direct comparison with the shock-free case, so that differences in ignition behaviour can be attributed primarily to shock-induced changes in the velocity, density and thermochemical fields.

It is recalled here that in order to obtain those predicted post-shock values, the inlet conditions are calculated as stated in § 2.1 through the ideal flow formulation, with selected studied cases gathered in table 1 and depicted in figure 2(*b*). Specifically, the modification of the incident shock intensity through variation of σ_i is addressed in order to analyse the competing effects of the arising reflected structures and the chemical kinetics. The analysis of the shock-wave effect and induced structures is addressed through variation of the incident angle (cases 3–6) and shock impingement distance (cases 7 and 8) from the inlet of the computational domain.

5.1. *Incident shock angle comparison*

The variation of the oblique shock angle implies a relative and consistent change of T_1 and T_2 to achieve the aforementioned values of T_3 and T_4. In turn, the reflected expansion arising from the resulting configuration of mechanical equilibrium has a wide range of intensities depending on the selection of σ_i, leading to relevant changes of temperature and Mach number behind this reflected wave (M_5, T_5) along the upper stream. Therefore, the cooling effect of the sudden expansion over the initiation of the reaction must be considered in shock-assisted ignition studies. The range of σ_i angles in this work is constrained to the surroundings of the limiting value that restrains ignition, $\sigma_i \simeq 36°$. In fact, the temperature fields of figure 12 show that the reactive mixing layer is ignited for the $\sigma_i = 35°$ configuration, while it is unable to react in the given domain length for $\sigma_i = 37.5°$. The black solid lines parallel to the deflected mixing layer placed at an unperturbed position are used to compare the temperature evolution along the upper stream behind the shock, represented in figure 13(*a*) for various oblique shock angles. It should be noted that the same post-shock temperatures are achieved in all cases ($T_3 = 1250$ K), but the reflected expansion is more intense as the incident shock angle is increased. This behaviour leads to an upper stream that is further cooled down; dashed lines represent the ideal-flow solution behind the expansion, which eventually does not enable the mixture to achieve auto-ignition in the given distance. In fact, the secondary expansions arising in the flow modify the expected post-shock stream temperature, and render invalid first-order estimates of ignition based on ideal shock mixture temperature.

Finally, the computed ignition distances are gathered in figure 13(*b*) for cases 3–5 with either tanh or self-similar inlet profiles, using the different species production–consumption criteria presented above with a 99.9 % percentile threshold. Note that the ignition distance decreases when employing the self-similar profile, whereas increasing σ_i progressively delays the ignition event, leading to failure (i.e. no ignition within the computational domain) for the hyperbolic tangent profile with $\sigma_i = 37.5°$. Case 6, with $\sigma_i = 40°$, is not presented here since ignition does not occur for either inlet profile configuration.

The results of case 5 for a limiting shock incident angle $\sigma_i = 37.5°$ with different inlet profiles are compared in figures 14(*a*,*b*). The computational data in this case induce us to think that the self-similar effects do constitute a requirement for achieving ignition. In the hyperbolic tangent case, the auto-ignition point cannot be calculated because a continuous ignition zone has not yet been formed, but weak isolated reactive kernels that are washed

https://doi.org/10.1017/jfm.2026.11936 Published online by Cambridge University Press

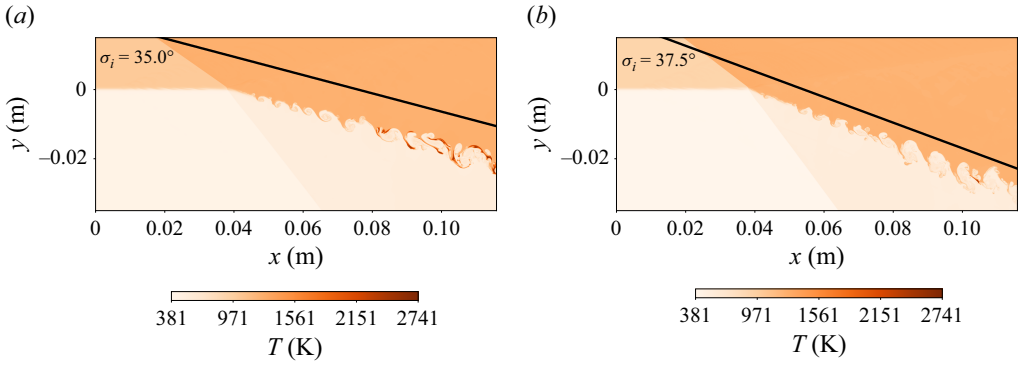


Figure 12. Temperature distribution with oblique shock impingement: (*a*) case 4 with $\sigma_i = 35°$, and (*b*) case 5 with $\sigma_i = 37.5°$, for hyperbolic tangent inlet profiles.

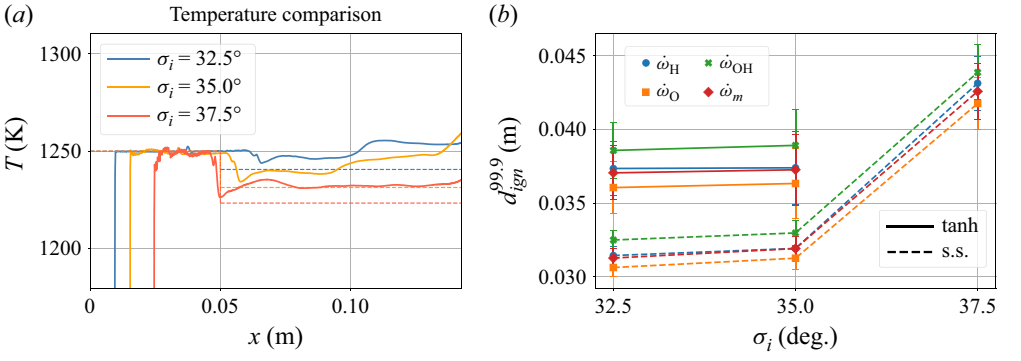


Figure 13. (*a*) Post-shock temperature evolution of the upper stream in the simulated cases (solid lines) and the corresponding ideal solution (dashed line). (*b*) Auto-ignition averaged distance d_{ign} for different production-rate criteria.

away are produced. In fact, the mean temperature and H_2 mass fraction profiles along the marked solid black line perpendicular to the mixing layer, placed before the auto-ignition position, are plotted in figure 14(*c*). This comparison shows an slightly greater amount of averaged H_2 concentration in the hot side of the self-similar case. However, given the barely appreciable difference between the two cases, figure 14(*d*) displays the mixedness of these profiles along the mixing layer, following the definition in Yu *et al.* (2020) and Li *et al.* (2020):

$$\xi(x) = \frac{1}{Y_{H_2,0}^2 H} \int_{H_y} 4 Y_{H_2} \left(Y_{H_2,0} - Y_{H_2} \right) \mathrm{d}y, \tag{5.1}$$

where H is the height of the selected subdomain. Thus it can be noticed that the mixing in the self-similar case develops from a higher value than in the hyperbolic tangent configuration. As the latter advances in space, it achieves the same mixing as in the self-similar case with a certain delay. However, it does so under further developed conditions of vorticity and stretching, which prevents the flame from effectively remaining anchored at a fixed ignition distance.

https://doi.org/10.1017/jfm.2026.11936 Published online by Cambridge University Press

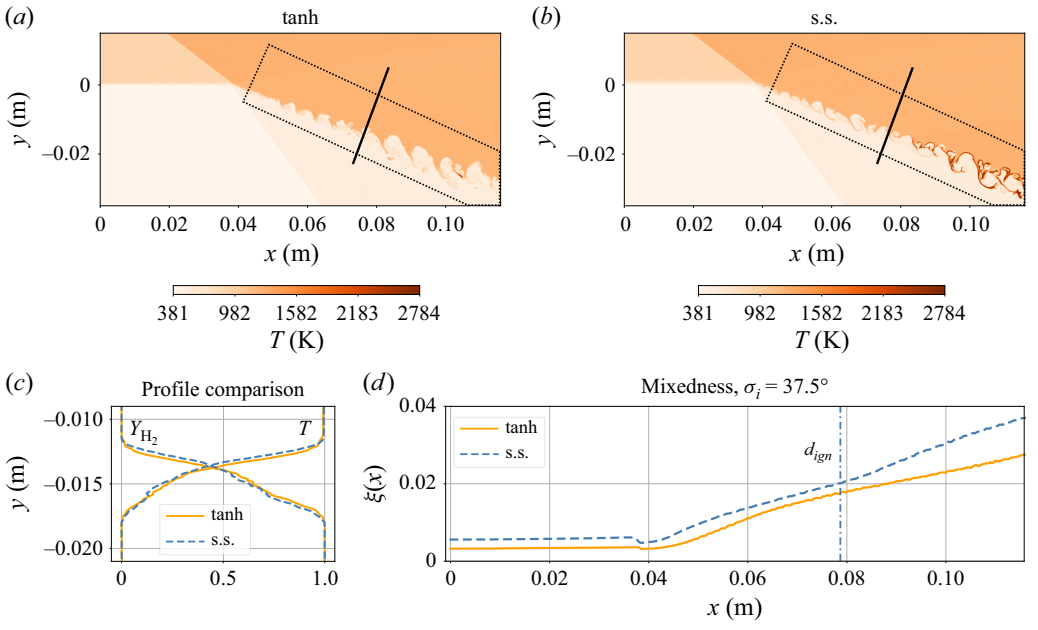


Figure 14. Temperature distribution of case 5 with (*a*) tanh and (*b*) self-similar inlet profiles. (*c*) Comparison of time-averaged temperature and mass fraction profiles over the marked black transverse line across the mixing layers. (*d*) Mixedness evolution along the longitudinal coordinate.

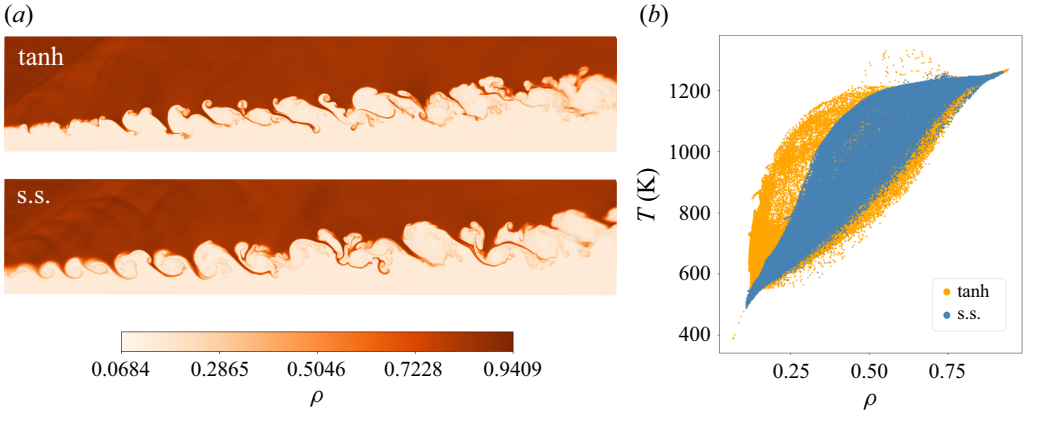


Figure 15. (*a*) Density fields of case 5 at the dotted subdomain marked in figures 14(*a*) and 14(*b*) before the completion of the numerical ignition transient, and (*b*) their associated snapshot temperature–density scatter plot.

We will then inspect the flow field during the transient regime, between the inert flow initial condition and the start of the chemical reaction. The density distributions of the post-shock region in the tanh and self-similar cases are presented in figure 15(*a*), showing small differences to visual inspection. The subdomain of analysis constitutes a fraction of the computational domain, which is highlighted in figures 14(*a*) and 14(*b*) with dotted rectangles. The lower level of mixing quality of the hyperbolic tangent case can also be observed in the density–temperature scatter in figure 15(*b*), extracted from the density

https://doi.org/10.1017/jfm.2026.11936 Published online by Cambridge University Press

fields in figure 15(*a*). For the same levels of temperature, a wider range of densities is observed in the tanh case. This indicates a stronger persistence of unmixed H_2 (low density) and air (higher density) streams, which later fail to ignite, in contrast with the self-similar reaction success.

In light of these results, the conclusion regarding the primary influence of inlet-prescribed mixing is reinforced. Subtle variations in the selected far-field characteristic conditions and in the inner-region profiles of the incoming mixing layer significantly affect the qualitative behaviour of the chemical reaction in supersonic hydrogen–air co-flows. These effects are fundamentally governed by enhanced mass diffusion and viscous dissipation, both of which must be consistently represented at the inlet.

5.2. *Effect of the shock impingement distance*

From an external inert perspective, the distance at which the shock impinges on the mixing layer does not affect the post-interaction equilibrium properties of the streams. However, when considering the inner region of the reactive mixing layer, with the mixing-layer thickness increasing and where reactions are promoted by mass diffusion and heat flux, it becomes evident that the shock impingement distance can directly influence the aerothermal properties inside the layer that are relevant to the local auto-ignition process. This effect is of paramount importance in scramjet design, where the combustion chamber configuration must ensure reliable ignition, so a robust performance must be maintained not only under varying shock angles but also for different impingement distances.

To measure the impact of this effect, the impingement distance d_{imp}, defined as the distance from the inlet domain and normalised by the initial vorticity thickness δ^0_ω, is varied while keeping the external thermodynamic conditions unchanged. The results are shown in figures 16(*a–c*) for $\sigma_i = 35^\circ$ and $d_{imp} = 20\delta^0_\omega$, $d_{imp} = 50\delta^0_\omega$ and $d_{imp} = 70\delta^0_\omega$, respectively, where the two-dimensional temperature fields are displayed for comparison. It can be observed that the further the impingement, the smaller the ignition distance d_{ign}, measured from the shock intersection. The ignition location is computed again with the 99.9 % percentile of $\dot{\omega}_m$, and presented in the $d^{99.9}_{ign} - y^{99.9}_{ign}$ plane in figure 16(*d*), with a confirmed trend of post-shock ignition distance reduction for increasing impingement distance. Note that although the simulations shown in figures 16(*a–c*) are all prescribed by the hyperbolic tangent profile, the computed distances also show the results of the case studies for the self-similar inlet profiles with empty markers, with both inlet conditions showing equivalent trends. The comparison between the two inflows shows that the auto-ignition distance remains virtually unchanged for $d_{imp} = 20\,\delta^0_\omega$, with relative error 1.6 % when changing the inlet profile. In the intermediate $50\,\delta^0_\omega$ case, the difference in the auto-ignition distance depending on the profile rises to 7.25 %, which remains comparable to the $70\,\delta^0_\omega$ case, where the difference does not exceed 7.6 %.

This can be readily connected to the analysis of previous sections and explained by the fact that for longer impingement distances, the mixing layer has more time to develop before the shock compression. The streamwise distribution of the mixedness factor $\xi(x)$ is presented in figure 16(*e*), where the pre-shock behaviour is identical for all the cases, and the post-shock contraction triggers more intense mixing dynamics for further impingement distances. As a result, the post-shock temperature rise occurs under better-mixed conditions, reducing the post-shock ignition distance and thereby partially compensating the overall auto-ignition process.

https://doi.org/10.1017/jfm.2026.11936 Published online by Cambridge University Press

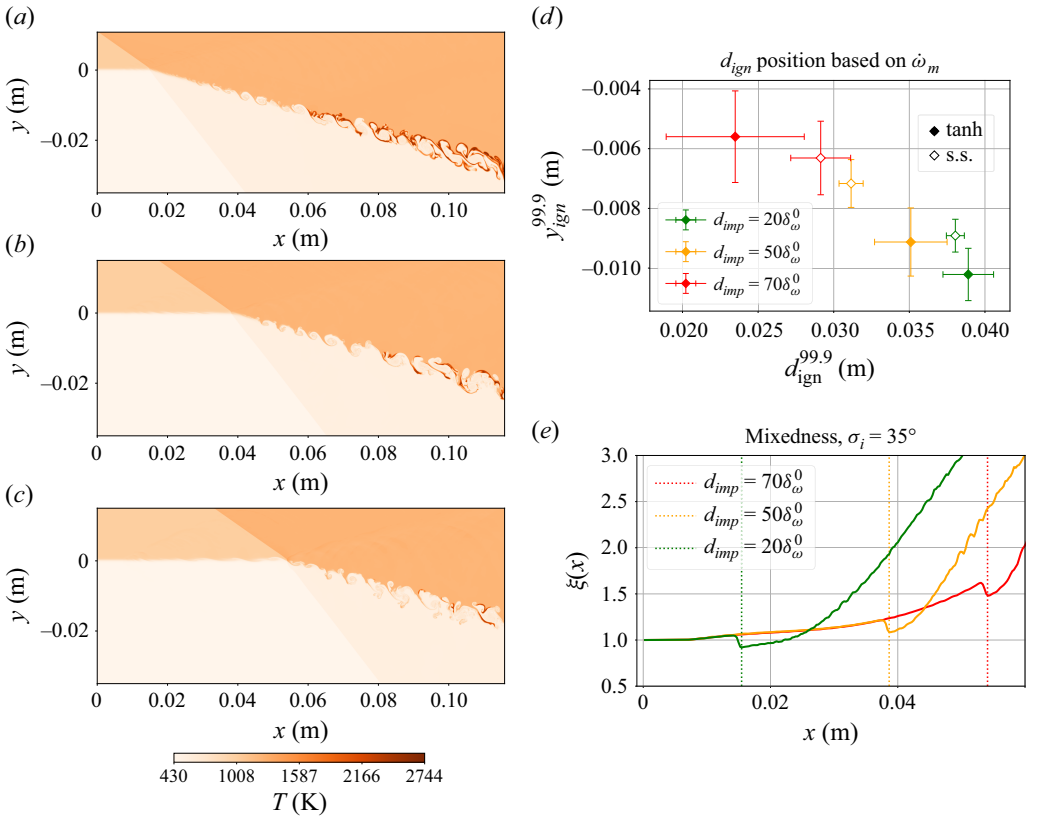


Figure 16. Temperature distribution of reactive mixing layers with oblique shock at $\sigma_i = 35°$ impinging at (*a*) $20\,\delta^0_\omega$, (*b*) $50\,\delta^0_\omega$ and (*c*) $70\,\delta^0_\omega$. Comparison of (*d*) auto-ignition averaged distances d_{ign} and (*e*) streamwise evolution of mixedness.

6. Concluding remarks

The analysis presented in this work focuses on the flow–structure effects on the auto-ignition processes of supersonic hydrogen–air mixing layers in two-dimensional configurations. The evolution of the reactive process is key to providing accurate predictions of the combustor performance in e.g. scramjet engines. This evolution is here addressed through a canonical approach, highlighting the intricate connections between the external flow field, shock-wave interactions, numerical boundary conditions and the inner region of the slender mixing layer. Based on the numerical analysis, the following concluding remarks can be made.

In shock-free conditions, the comparison between standard hyperbolic tangent profiles and self-similar profiles (which account for detailed physical processes like Soret, Dufour and viscous dissipation) yield distinct behaviours depending on the external thermal configuration.

(i) In the case of non-isothermal (hot–cold) streams, where the air stream was significantly hotter ($T_1 = 1250$ K, $T_2 = 545$ K), the auto-ignition distance was found to be virtually unchanged by the inlet profile choice, suggesting that the ignition event is primarily thermally controlled. Nevertheless, the inclusion of realistic mass diffusion in the self-similar profiles caused the vertical position of the ignition kernel

https://doi.org/10.1017/jfm.2026.11936 Published online by Cambridge University Press

(y_{ign}) to double, shifting the ignition location towards the hot stream, where high temperature coexists with greater amounts of fuel.

(ii) For isothermal streams, with both streams at $T_1 = T_2 = 1250$ K, the self-similar profile predicted a significantly shorter auto-ignition distance compared to the hyperbolic tangent case, reducing d_{ign} by over 1 cm; this acceleration of the auto-ignition event is explicitly attributed to the temperature increase due to thermal viscous dissipation included in the self-similar profiles, which enhances the reaction without substantially affecting the overall flow field or vorticity thickness scale.

For shock-assisted ignition of supersonic mixing layers, the analysis was conducted such that the post-shock conditions matched those of the reference non-isothermal case ($M_3 = 2.0,\ \ T_3 = 1250\,\text{K};\ M_4 = 1.25,\ \ T_4 = 545\,\text{K}$), enabling the assessment of shock-induced flow structures, including the transmitted shock and reflected wave. Increasing the incident shock angle (σ_i) is known to intensify the reflected expansion wave, which locally cools down the upper stream (denoted as region 5) and progressively delays the ignition distance d_{ign}, causing the complete failure of the ignition event for larger angles ($\sigma_i = 40°$). In marginal cases, found at $\sigma_i = 37.5°$, self-similar dissipative effects are necessary to achieve continuous ignition, as the hyperbolic tangent profile produces only isolated kernels that are washed away downstream, whereas the self-similar profile, starting from a higher initial mixedness value, allows the flame to anchor effectively at a fixed distance. It was also observed that the further downstream the shock impingement point is located, the closer the final ignition point is to the wave intersection, a behaviour that is attributed to the mixing layer having more time to develop and reach a better-mixed state before the post-shock temperature rise occurs.

Overall, the present study contributes to a deeper physical understanding of combustion and auto-ignition phenomena in supersonic hydrogen–air mixing-layer configurations of direct relevance to high-speed propulsion concepts. We demonstrate that ignition is not solely dictated by post-shock thermochemical states, but is strongly affected by the internal structure of the developing layer and by the flow-induced structures – e.g. shock transmission, reflected expansions, and their intersection – that modulate it. In particular, the level of mixedness and the inclusion of thermal processes can decisively control the onset of ignition and thus the resulting flame anchoring distances. The results show that seemingly minor modelling and inflow choices – e.g. the degree of premixing embedded in the inlet profiles and the inclusion of dissipative/diffusive mechanisms – can appreciably shift the ignition kernel location by a measurable margin, or determine whether ignition anchors continuously, remains intermittent in marginal regimes or fails (e.g. with $\sigma_i \gtrsim 37.5°$ for the parametric combination selected here). These sensitivities highlight the undeniable and important limitation of two-dimensional canonical set-ups when extrapolating ignition lengths to practical devices.

The present simulations are restricted to a two-dimensional DNS framework, focused on the fundamental aspects of ignition before including the effects of turbulent fluctuations and flame–turbulence interactions, and therefore do not explicitly account for three-dimensional mechanisms such as vortex stretching, enhanced scalar dissipation rates or small-scale intermittency, which is known to influence auto-ignition in practical systems. In a fully turbulent three-dimensional mixing layer, small-scale structures would generally undergo rapid breakdown due to turbulent mixing and enhanced scalar dissipation. This would tend to reduce the direct influence of the boundary layer profiles introduced by the self-similar solutions imposed at the inlet. In the present configuration, the convective Mach number reaches $M_c \simeq 0.56$, which lies close to the regime where compressibility effects become significant. Previous studies (e.g. Sandham & Reynolds

https://doi.org/10.1017/jfm.2026.11936 Published online by Cambridge University Press

1990; Clemens & Mungal 1992) indicate that three-dimensionality becomes dominant for $M_c \simeq 0.6$, suggesting that the present cases are near a transitional regime. Based on this, it is expected that while three-dimensional turbulence would modify the quantitative details of ignition (e.g. ignition delay and location), the qualitative sensitivity to the inlet flow structure identified here may still persist, particularly in high-speed flows, where compressibility effects preserve large-scale fluctuations and reduce mixing efficiency.

Future work should therefore extend the framework to fully three-dimensional layers and inflow profiles with realistic turbulent content and integral scales, so as to quantify how robust the identified mechanisms are under three-dimensional instabilities, turbulent mixing scales and turbulence-driven intermittency, and to provide ignition-distance predictions with improved transferability to scramjet-relevant scenarios.

Acknowledgements. While finishing this study, we were deeply saddened to learn of the passing of Professor A. Liñán. He passed away on 8 November 2025, at the age of 90, leaving behind a wide community of combustion scientists and fluid dynamicists whom he helped shape. Some of the authors had the privilege of knowing him personally, and gratefully acknowledge his guidance and his science-first mindset, consistently seeking understanding while remaining indifferent to personal acclaim. He will be profoundly missed.

Funding. The work of N.G.C. was supported by project TED2021-129446B-C43 funded by Agencia Estatal de Investigación MCIN/AEI/10.13039/501100011033. The work of C.H. was supported by project PID2022-139082NB-C51 funded by MICIN/AEI/10.13039/501100011033/FEDER, UE. This work was also supported in part by MCIN/AEI/10.13039/501100011033 and ESF/10.13039/501100004895 (grant no. RYC2019-027592-I) for P.J.M.-F. The work of D.M.-R. was supported by project PID2023-150646NB-I00, funded by Agencia Estatal de Investigación MICIU/AEI/10.13039/501100011033 and ERDF/EU.

Declaration of interests. The authors report no conflict of interest.

Author contributions. N.G.C. curated and validated the data, produced the visualisations, contributed to developing the software, and wrote the original draft. P.J.M.-F. developed the software, contributed to the methodology, and reviewed the manuscript. D.M. contributed to the methodology, supervised the work, reviewed and edited the manuscript, and acquired funding. C.H. contributed to the conceptualisation and methodology, wrote parts of the manuscript, reviewed it, and acquired funding. D.M.-R. led the conceptualisation and methodology, supervised the project, wrote and edited the manuscript, and acquired funding.

Data availability statement. The data that support the findings of this study are available from the authors upon reasonable request.

References

Abdulrahman, G.A.Q., Qasem, N.A.A., Imteyaz, B., Abdallah, A.M. & Habib, M.A. 2023 A review of aircraft subsonic and supersonic combustors. *Aerosp. Sci. Technol.* **132**, 108067.

Bao, W., Duan, Y., Zhou, W. & Yu, D. 2014 Hydrogen-fueled scramjet cooling system investigation using combustor and regenerative cooling coupled model. *Proc. Part G: J. Inst. Mech. Engng G: J. Aerosp. Engng* **228** (6), 820–830.

Barre, S. & Bonnet, J.-P. 2015 Detailed experimental study of a highly compressible supersonic turbulent plane mixing layer and comparison with most recent DNS results: 'towards an accurate description of compressibility effects in supersonic free shear flows'. *Intl J. Heat Fluid Flow* **51**, 324–334.

Barre, S., Quine, C. & Dussauge, J.P. 1994 Compressibility effects on the structure of supersonic mixing layers: experimental results. *J. Fluid Mech.* **259**, 47–78.

Boukharfane, R. 2025 Modal analysis of oblique shock-induced flow dynamics in a supersonic reacting shear layer. arXiv:2505.07636.

Brummund, U. & Nuding, J. 1997 Interaction of a compressible shear layer with shock waves – an experimental study. In *35th Aerospace Sciences Meeting and Exhibit, AIAA Meeting Papers*, 97-0392. American Institute of Aeronautics and Astronautics.

Buttsworth, D.R. 1996 Interaction of oblique shock waves and planar mixing regions. *J. Fluid Mech.* **306**, 43–57.

https://doi.org/10.1017/jfm.2026.11936 Published online by Cambridge University Press

CHENG, T.S., WEHRMEYER, J.A., PITZ, R.W., JARRETT, J. & NORTHAM, G.B. 1994 Raman measurement of mixing and finite-rate chemistry in a supersonic hydrogen–air diffusion flame. *Combust. Flame* **99** (1), 157–173.

CLEMENS, N.T. & MUNGAL, M.G. 1992 Two-and three-dimensional effects in the supersonic mixing layer. *AIAA J.* **30** (4), 973–981.

DA RIVA, I., LIÑÁN MARTÍNEZ, A. & FRAGA, E. 1964 Some results in supersonic combustion. In *Advances in Aeronautical Sciences: Proceedings of the Fourth International Congress in the Aeronautical Sciences, Paris, 24–28 August 1958*. ICAS.

DINESH, K.K.J.R., SHALABY, H., LUO, K.H., VAN OIJEN, J.A. & THÉVENIN, D. 2016 Effects of pressure on cellular flame structure of high hydrogen content lean premixed syngas spherical flames: a DNS study. *Intl J. Hydrogen Energy* **41** (46), 21516–21531.

DRUMMOND, J.P. 1988 Numerical simulation of a supersonic chemically reacting mixing layer. *NASA Tech. Rep.* TM 4055.

FERRER, P.J.M., LEHNASCH, G. & MURA, A. 2012 Direct numerical simulations of high speed reactive mixing layers. *J. Phys.: Conf. Ser.* **395**, 012004.

FERRI, A., LIBBY, P.A. & ZAKKAY, V. 1964 Theoretical and experimental investigation of supersonic combustion. In *High Temperatures in Aeronautics, Proceedings of the Symposium Held in Turin to Celebrate the 50th Anniversary of the Laboratorio di Aeronautica, Politecnico di Torino, 10–12 September 1962*, pp. 55–118. Elsevier.

GAITONDE, D.V. 2015 Progress in shock wave/boundary layer interactions. *Prog. Aerosp. Sci.* **72**, 80–99.

GAITONDE, D.V. & ADLER, M.C. 2023 Dynamics of three-dimensional shock-wave/boundary-layer interactions. *Annu. Rev. Fluid Mech.* **55** (1), 291–321.

GROSS, R.A. & CHINITZ, W. 1960 A study of supersonic combustion. *J. Aerosp. Sci.* **27** (7), 517–524.

GUTMARK, E.J., SCHADOW, K.C. & YU, K.H. 1995 Mixing enhancement in supersonic free shear flows. *Annu. Rev. Fluid Mech.* **27** (1), 375–417.

HUETE, C., SÁNCHEZ, A.L. & WILLIAMS, F.A. 2017 Diffusion-flame ignition by shock-wave impingement on a hydrogen–air supersonic mixing layer. *J. Propul. Power* **33** (1), 256–263.

HUETE, C., SÁNCHEZ, A.L., WILLIAMS, F.A. & URZAY, J. 2015 Diffusion-flame ignition by shock-wave impingement on a supersonic mixing layer. *J. Fluid Mech.* **784**, 74–108.

HUETE, C., URZAY, J., SÁNCHEZ, A.L. & WILLIAMS, F.A. 2016 Weak-shock interactions with transonic laminar mixing layers of fuels for high-speed propulsion. *AIAA J.* **54** (3), 966–979.

IM, H.G., CHEN, J.H. & LAW, C.K. 1998 Ignition of hydrogen–air mixing layer in turbulent flows. *Symp. (Intl) Combust.* **27** (1), 1047–1056.

JU, Y. & NIIOKA, T. 1994 Reduced kinetic mechanism of ignition for nonpremixed hydrogen/air in a supersonic mixing layer. *Combust. Flame* **99** (2), 240–246.

KLEIN, M., HERBERT, A., KOSAKA, H., BÖHM, B., DREIZLER, A., CHAKRABORTY, N., PAPAPOSTOLOU, V., IM, H.G. & HASSLBERGER, J. 2020 Evaluation of flame area based on detailed chemistry DNS of premixed turbulent hydrogen–air flames in different regimes of combustion. *Flow Turbul. Combust.* **104** (2), 403–419.

KOURTA, A. & SAUVAGE, R. 2002 Computation of supersonic mixing layers. *Phys. Fluids* **14** (11), 3790–3797.

LANDAU, L.D. & LIFSHITZ, E.M. 1966 *Fluid Mechanics*, 3rd edn. Pergamon Press.

LEEP, L.J., DUTTON, J.C. & BURR, R.F. 1993 Three-dimensional simulations of compressible mixing layers: visualizations and statistical analysis. *AIAA J.* **31** (11), 2039–2046.

LI, Y., WANG, Z., YU, B., ZHANG, B. & LIU, H. 2020 Gaussian models for late-time evolution of two-dimensional shock–light cylindrical bubble interaction. *Shock Waves* **30** (2), 169–184.

LIBBY, P.A. 1962 Theoretical analysis of turbulent mixing of reactive gases with application to supersonic combustion of hydrogen. *Am. Rocket Soc. J.* **32** (3), 388–396.

LIU, Q., BACCARELLA, D. & LEE, T. 2020 Review of combustion stabilization for hypersonic airbreathing propulsion. *Prog. Aerosp. Sci.* **119**, 100636.

MARBLE, F.E. 1994 Gasdynamic enhancement of nonpremixed combustion. *Proc. Combust. Inst.* **25**, 1–12.

MARTÍNEZ-FERRER, P.J., BUTTAY, R., LEHNASCH, G. & MURA, A. 2014 A detailed verification procedure for compressible reactive multicomponent Navier–Stokes solvers. *Comput. Fluids* **89**, 88–110.

MARTÍNEZ-RUIZ, D., HUETE, C., MARTÍNEZ-FERRER, P.J. & MIRA, D. 2019 Irregular self-similar configurations of shock-wave impingement on shear layers. *J. Fluid Mech.* **872**, 889–927.

MARTÍNEZ-RUIZ, D., HUETE, C., SÁNCHEZ, A.L. & WILLIAMS, F.A. 2018 Interaction of oblique shocks and laminar shear layers. *AIAA J.* **56** (3), 1023–1030.

https://doi.org/10.1017/jfm.2026.11936 Published online by Cambridge University Press

McMullan, W.A., Gao, S.C.C.M. & Coats, C.M. 2007 A comparative study of inflow conditions for two- and three-dimensional spatially developing mixing layers using large eddy simulation. *Intl J. Numer. Meth. Fluids* **55** (6), 589–610.

Menon, S. & Fernando, E. 1990 A numerical study of mixing and chemical heat release in supersonic mixing layers. In *28th Aerospace Sciences Meeting*, p. 152. American Institute of Aeronautics and Astronautics.

Moeckel, W.E. 1952 Interaction of oblique shock waves with regions of variable pressure, entropy, and energy. *NACA Tech. Rep.* TN 2725.

Nishioka, M. & Law, C.K. 1997 A numerical study of ignition in the supersonic hydrogen/air laminar mixing layer. *Combust. Flame* **108** (1–2), 199–219.

Nordin-Bates, K., Fureby, C., Karl, S. & Hannemann, K. 2017 Understanding scramjet combustion using LES of the HyShot II combustor. *Proc. Combust. Inst.* **36** (2), 2893–2900.

Qiao, H., Zhang, L., Guo, J., Wang, J., Im, H.G., Liang, J. & Zhou, Z. 2025 LES of supersonic non-premixed combustion using a Lagrangian FMDF approach. *Proc. Combust. Inst.* **41**, 105887.

Rogers, M.M. & Moser, R.D. 1994 Direct simulation of a self-similar turbulent mixing layer. *Phys. Fluids* **6** (2), 903–923.

Rosner, D.E. 2012 *Transport Processes in Chemically Reacting Flow Systems*. Courier Corporation.

Sandham, N.D. & Reynolds, W.C. 1989 Some inlet-plane effects on the numerically simulated spatially-developing mixing layer. In *Turbulent Shear Flows 6: Selected Papers from the Sixth International Symposium on Turbulent Shear Flows, Université Paul Sabatier, Toulouse, France, September 7–9, 1987*, pp. 441–454. Springer.

Sandham, N.D. & Reynolds, W.C. 1990 Compressible mixing layer – linear theory and direct simulation. *AIAA J.* **28** (4), 618–624.

Sarkar, S. 1995 The stabilizing effect of compressibility in turbulent shear flow. *J. Fluid Mech.* **282**, 163–186.

Strang, G. 1968 On the construction and comparison of difference schemes. *SIAM J. Numer. Anal.* **5** (3), 506–517.

Sánchez, A.L. & Williams, F.A. 2014 Recent advances in understanding of flammability characteristics of hydrogen. *Prog. Energy Combust. Sci.* **41**, 1–55.

Sánchez, A.L., Fernández-Tarrazo, E., Boivin, P., Liñán, A. & Williams, F.A. 2012 Ignition time of hydrogen–air diffusion flames. *C. R. Méc.* **340** (11–12), 882–893.

Tang, T., Sun, M., Yan, B., Wang, Z., Yu, J., Huang, Y., Wang, H. & Zhu, J. 2024*a* Flow structures and combustion regimes in an axisymmetric scramjet combustor with high Reynolds number. *J. Fluid Mech.* **1000**, A3.

Tang, T., Wang, Z., Yu, J., Huang, Y., Sun, M., Wang, H., Zhao, G., Yang, Y. & Xiong, D. 2024*b* Investigation of multi-scale flow structures and combustion characteristics in a cavity-enhanced circular scramjet. *Combust. Flame* **264**, 113431.

Techer, A., Lehnasch, G., Mura, A. & Moule, Y. 2015 Large eddy simulations of combustion in a supersonic Mach 2 transverse flow. In *20th AIAA International Space Planes and Hypersonic Systems and Technologies Conference*, p. 3543. American Institute of Aeronautics and Astronautics.

Tian, Y., Bai, Y., Zhao, Q., Chong, D. & Yan, J. 2025 Direct numerical simulation of turbulent mixing in supersonic coflow jets. *Phys. Fluids* **37** (2), 025192.

Treviño, C. & Liñán, A. 1995 Mixing layer ignition of hydrogen. *Combust. Flame* **103** (1–2), 129–141.

Tsujikawa, Y. & Northam, G.B. 1996 Effects of hydrogen active cooling on scramjet engine performance. *Intl J. Hydrogen Energy* **21** (4), 299–304.

Urzay, J. 2018 Supersonic combustion in air-breathing propulsion systems for hypersonic flight. *Annu. Rev. Fluid Mech.* **50** (1), 593–627.

Wei, J., Zhu, X. & Wang, N. 2025 Examination of differential diffusion effects in spatially-developing supersonic mixing layer hydrogen flames. *Combust. Flame* **276**, 114138.

Xie, H., Zhang, D., Tan, J., Ding, M. & Wang, Y. 2025 Structural evolution and modal property of the supersonic mixing layer downstream of a splitter plate. *Aerosp. Sci. Technol.* **168**, 110871.

Yu, B., He, M., Zhang, B. & Liu, H. 2020 Two-stage growth mode for lift-off mechanism in oblique shock-wave/jet interaction. *Phys. Fluids* **32** (11), 116105.

Yu, T. & Chen, Q. 2025 Mixing enhancement in direct numerical simulation of shock wave–mixing layer interaction for aerospace propulsion. *Acta Astronaut.* **238**, 839–855.

Zhang, D., Tan, J. & Yao, X. 2021 Vortex evolution and flame propagation driven by oblique shock wave in supersonic reactive mixing layer. *Aerosp. Sci. Technol.* **118**, 106993.

https://doi.org/10.1017/jfm.2026.11936 Published online by Cambridge University Press